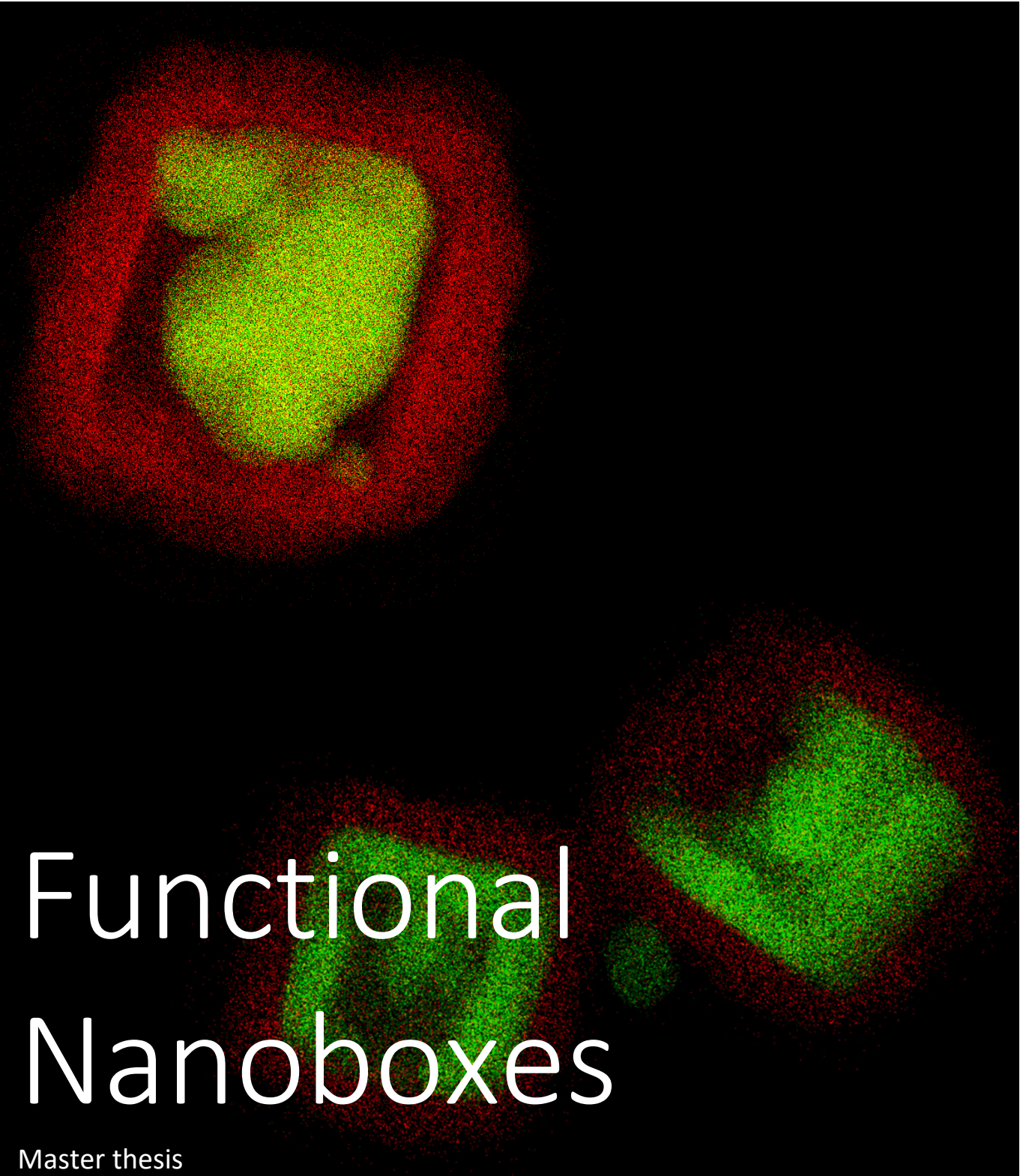

Functional Nanoboxes

Master thesis

July 26, 2019

Sprockel, A.J. (Alessio)
UTRECHT UNIVERSITY - PHYSICAL CHEMISTRY AND COLLOIDS

Under the supervision of
F. Dekker & Prof A. P. Philipse

DSM
BRIGHT SCIENCE. BRIGHTER LIVING.

NWO | Applied and Engineering Sciences

This project was funded by NWO (TTW) under project number 14210

Abstract

In this work, the preparation of mesoporous silica nanoboxes is presented for application in optical thin films. Mesoporous silica nanoboxes are obtained by coating cuprous oxide nanocubes with MCM-41 silica and subsequently dissolving the core. The thickness of the shell can be controlled by varying the silica precursor concentration. The surface area and pore size are quantified using N_2 absorption. Filling the hollow particles with functional material, allows the boxes to become functional, without changing their colloidal stability. Two approaches were attempted to produce functional nanocubes. The seeded growth of gold nanoparticles proved to be problematic, as nucleating occurs randomly on the most favorable positions. Gold deposits were found on the outside of the wall and in the mesopores. Transformation of the Cu_2O core into functional materials proved to result in well-defined particles. The cuprous oxide template was transformed to a copper core via “in liquid thermolysis”. Subsequently, the copper core was transformed into a silver or a gold core via galvanic displacement. The functionality of the silver core is confirmed by following the catalytic degradation of congo red dye via UV-Vis over time.

Porous and functional nanoboxes

1. Introduction

Nowadays, colloids can be prepared with different sizes, shapes and functionalities[1]. Specific functionality is often coupled to a specific shape. The shape of the particle influences the structure formed during self-assembly[2-4], and it is known that the plasmonic properties of silver nanoparticles are determined by their shape[5]. Functionalizing particles without changing their shape or colloidal stability is still a challenge in colloidal synthesis. To overcome this challenge, preparation methods are required that introduce functionality without changing surface properties. A well-known method to do this is the preparation of core-shell particles. Spherical core-shell particles can be prepared[6], but the synthesis of anisotropic core-shell particles is still a challenge. This project investigates the possibility of the synthesis of mesoporous silica nanoboxes and the deposition of a functional material inside while preserving the cubic shape. The advantage of the core-shell design is that the interior of the nanoboxes can be functionalized without changing the changing the surface of the particles, therefore retaining their shape-specific properties. The functional nanoboxes can provide a relatively easy route to provide additional functionally to silica nanoboxes, which are suitable to prepare thin-film anti-reflective coatings. In this design, the low refractive index properties of the box allow for antireflective properties of the coating, while an internal material provides, for instance, anti-fouling properties.

Since W. Stöber synthesized silica spheres in 1968[7], several adjustments have been made to the Stöber method in attempts to synthesize silica colloids of specific morphology[8,9]. Coating a template followed by template removal, has become a popular method to synthesize hollow colloids[9]. Using templates, porous hollow microspheres can be obtained with tunable size, wall thickness and porosity[10,11]. Progress has already been made in functionalizing spherical hollow colloids[12], and advancements within our group led to the preparation of hollow silica nanocubes[13]. Functional hollow spherical colloids show potential in catalysis, where the incorporation of noble metals inside silica colloids shows potential in terms of increased performance, stability and recoverability[14]. In medicine, the core-shell design is employed as a drug delivery device, enabling the transport of sensitive drugs to the cell interior[15].

The proposed research of anisotropic functional core-shell colloids will allow the decoupling of the form and the function in the field of colloid science. Benefiting from the characteristic of a stable silica cubic shell, and having the freedom to functionalize the internal void. Overall the design provides new opportunities to the growing number of colloidal applications.

In this thesis we will present a method to produce functional mesoporous nanoboxes of circa 120 nm. To achieve this, first stable mesoporous nanoboxes should be obtained with control over wall thickness and porosity. To produce functional nanoboxes, calcination is required, which often leads to reduced colloidal stability[16]. In-liquid calcination is used to retain colloidal stability after calcination. Finally, we will present a method to transform the cuprous oxide template and produce nanoboxes with a copper, silver and golden core. Catalytic dye degradation was used to confirm the functionality of the metal core.

2. Theory

Before we discuss functional nanoboxes, it is important to understand simple nanoboxes. Since the nanocubes are designed to find application in antireflective coatings (ARC), a short background is given on reflectivity and how thin films can reduce refection.

2.1. Antireflective coatings

2.1.1. Rayleigh's film

An early example of applying a film to reduce reflection was presented by Lord Rayleigh in the 19th century[17]. Rayleigh discovered that applying a tarnish to glass increased, instead of decreased, the transmittance of glass. The increased transmittance was caused by the gradual or stepwise change of refractive index, investigation of this phenomenon resulted in the development of anti-reflective coatings[17].

The fraction of light reflected (R_{01}), by traveling under normal incidence across a single interface is determined by:

$$R_{01} = \left(\frac{n_0 - n_s}{n_0 + n_s}\right)^2 . \quad (1)$$

Here n_0 is the refractive index of the incident medium and n_s the refractive index of the substrate. This reflection, named Fresnel reflection, is described by the Fresnel equations[18]. Following Equation 1 for the common example of visible light crossing an air-glass interface at normal incidence, where the refractive index n changes from air (n_o = 1.00) to glass (n_s = 1.52), circa 4.25% of light is reflected. In the instance of a simple glass window, where two interfaces are present, only 91.66% of light is transmitted[18].

A thin layer of material can be applied on the air-glass interface to reduce reflection. The calculation of the reflection of such a thin film system is less trivial than for single interface. For the transition between air (n_0) and glass (n_s), with an intermediate thin film (n_1) with thickness t the reflection (R) can be calculated using[18]:

$$R = \left(\frac{a_1 \cos^2 \delta + a_2 \sin^2 \delta}{a_3 \cos^2 \delta + a_4 \sin^2 \delta}\right) \quad (2)$$

$$a_1 = (n_0 - n_s)^2 \quad ; \quad a_2 = (n_1^2 - n_0 n_s)^2 \quad ; \quad a_3 = (n_0 + n_s)^2 \quad ; \quad a_4 = (n_1^2 + n_0 n_s)^2 \quad (3)$$

$$\delta = \frac{2\pi n_1 t}{\lambda} \quad (4)$$

Here λ is the wavelength of light in vacuum. Equation 2 reduces to Equation 1 if δ is equal to $n\pi$, and n_1 is equal to n_0 or n_s. When δ is equal to π/2, the equation simplifies to:

$$R = \left(\frac{n_1^2 - n_0 n_s}{n_1^2 + n_0 n_s}\right)^2 \quad (5)$$

In Equation 5 the optical thickness (t/n_1) is equal to a quarter of the wavelength. In Equation 5 it is easily visible that if n_1^2 is equal $n_0 n_s$, the reflection is zero. The ideal thin film thus has two properties; the refractive index is the geometric mean of the original interface materials, $n_{AR} = \sqrt{n_0 n_S}$, and the thickness is equal a quarter of the light wavelength in the thin film, $t = \lambda/4n_{AR}$.

For the interface between air and glass, the optimal thin film for red light (λ = 660 nm) has a refractive index of 1.23, with a thickness of 134 nm. For this optimal situation, all light is transmitted. The effectiveness of this thin film is reduced when the incoming light is not of the corresponding wavelength, or if the light crosses the interface at an oblique angle. The effectiveness of the thin film is also lowered if the refractive index of the coating deviates from the geometric mean. Although not all light is transmitted in these non-ideal situations, transmittance is still higher than for a bare glass substrate.

2.1.2. Applications

Reduction of reflection is important for any technology that contains optics. Lenses, for instance greatly benefitting from the reduction of reflection. Reduction of reflection allows manufacturers to develop lens systems containing over 16 lenses without losing to much light. The light loss of a glass 16 element lens system (Figure 1) without any antireflective coating would result in the loss of at least 75% of incoming light, significantly reducing its applicability in optics. Additionally, these reflections also produce lens flare artifacts, reducing image quality.

Figure 1: 16 element Tamron 18-400mm F/3.5-6.3 Di II VC HLD lens[19].

Another application of anti-reflective coatings is in the field of solar cells. Any light reflected off the interfaces before photon absorption is lost energy. Since the efficiency of the solar panel is largely determined by light of a specific wavelength region, the anti-reflective coating can be optimized for a specific wavelength.

2.1.3. Coating requirements

The materials used for antireflective coatings is required to meet certain specifications depending on the targeted wavelength region and the properties of the interface. As discussed in 2.1.1 to optimally suppress the reflection, the material is required to have a refractive index that is the geometric mean of the base materials. Thus, to produce anti-reflection coating for an air-glass interface a material with a refractive index of 1.23 must be found or developed. With 1.38, MgF_2 has the lowest refractive index of the conventional solids, but this is still significantly above the ideal refractive index of 1.23. A proposed solution to this challenge is the use of porous materials. By increasing the porosity, the solid fraction of the material is reduced, in turn reducing the refractive index. Porous silica, for instance, could be obtained with a refractive index of 1.23.

If a material with a suitable refractive index can be found, a second requirement is to apply this material at a distinct thickness, often quarter wavelength thickness. In addition to the refractive index and thickness, several other, application specific, requirements may arise, including, scratch resistance, chemical resistivity and heat stability. To increase durability under outdoor exposure, anti-bacterial or anti-fungal functionality can be added to the coating to reduce biofouling.

To conclude, a general material suitable for use as an anti-reflective coating needs to possess a highly tunable refractive index and thickness. A proposed solution to the problem lies at the base of the first part of this research project, nanoboxes. In addition to their already hollow structure, silica nanoboxes can be prepared with mesoporous silica. The use of porous silica enables the ARC to have an even lower silica volume fraction, reducing its refractive index. In the next sections it will be discussed how nanoboxes can be produced and what challenges remain for their wide scale application.

The application of nanoboxes, or hollow nanoparticles in general, as anti-reflective coatings has been previously discussed[17,18]. The use of hollow nanoboxes adheres to the general feature found in ARCs, the use of a continuously changing refractive index and porous materials[18]. By varying the volume fraction between the internal void of the cube, the refractive index of the cube can be varied between the index of the solid and a refractive index of 1, for extremely porous materials. Using hollow silica particles allows the coating to reach lower refractive indices than usually obtainable . Hollow silica cubes could potentially provide a way to produce anti-reflective coatings of highly tunable refractive index and thickness. Since the cubes are the same material as the bare glass, problems with chemical and thermal stability are negated.

2.2. Porous nanoboxes

2.2.1. Templated silica nanoboxes

Because of the amorphous nature of silica, its growth cannot be promoted in a specific facet direction. The production of hollow anisotropic silica is, therefore, generally approached via a template technique[20]. For silica nanoboxes, a cubic template of the right size has to be produced first[13]. The template can then be coated with either microporous Stöber silica, or mesoporous MCM-41 silica. The template can afterwards be removed to obtain hollow anisotropic silica particles. An ideal template for nanoboxes with a size between 80 – 150 nm are cuprous oxide cubes. The gram scale synthesis of Cu_2O nanocubes was reported in 2009 by Park *et al*.[21]. Park used a polyol reduction to synthesize cuprous oxide cubes in the size range 50 – 100 nm. The use of cuprous oxide cubes as template for Stöber silica was demonstrated in our group[13]. To produce porous silica, an additional template is required. To distinguish between the two templates, the core cuprous oxide template is termed the *shape template*, while the template providing porosity is termed the *porosity template*.

2.2.2. Silica coating

Silica coatings have long been used on nanoparticles and are excellent in providing colloidal stability and chemical resilience[22]. The synthesis of silica nanoparticles was first reported by Stöber *et al.* in 1968 and similar silica synthesis techniques remain widely to produce silica coated nanoparticles[7]. Stöber *et al.* used tetra-esters of silicic acid as a precursor, which after ammonia catalyzed polymerization form an amorphous silica network. A typical precursor for Stöber silica is tetraethyl orthosilicate (TEOS). The reactions required for the formation of a network link are displayed in Reaction 1 and 2. The reaction starts with the hydrolysis of TEOS, followed by a condensation reaction.

$$Si(OEt)_4 + H_2O \rightarrow HO - Si(OEt)_3 + EtOH \qquad (Reaction\ 1)$$

$$(EtO)_3Si - OH + HO - Si(OEt)_3 \rightarrow (EtO)_3Si - O - Si(OEt)_3 + H_2O \qquad (Reaction\ 2)$$

The reaction rate is primarily limited by the hydrolysis rate, which is sensitive to dissolved base catalysts. During coating of nanoparticles with Stöber silica, oligomers form in solution, which aggregate and condensate on the particle surface. Since coating formation requires aggregation of oligomers on the surface, the nanoparticle surface has to be suitable for oligomer aggregation[23]. Since many different templates can be coated with Stöber silica, the method allows the preparation of a variety of anisotropic silica colloids. Not only colloidal templates proved suitable as a silica template, circa 25 years after the development of Stöber silica, Kresge *et al.* used ordered surfactant micelles as a template to produce mesoporous silica[24].

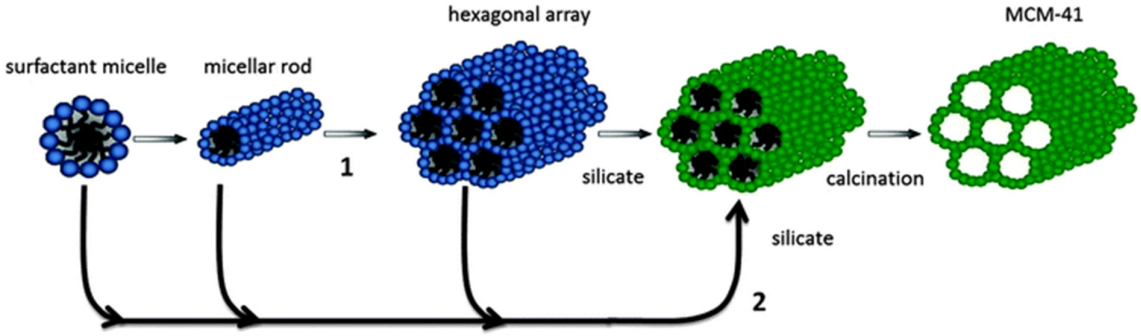

Figure 2: Graphical representation of MCM-41 formation[25].

By producing Stöber silica in high concentrations of CTAB micelles, the silica deposits around the ordered template. The hexadecyltrimethylammonium ions form tubular micelles with a diameter of circa 2 nm, which assemble in hexagonal arrays at high concentrations. These hexagonal arrays are ideal as mesoporous silica templates. CTAB templated silica was further developed by the Mobil Oil Corporation and is now commonly known as MCM-41 (Mobil Composition of Matter 41). A graphical representation of the production of MCM-41 is given in Figure 2.

As shown in the graphical representation in Figure 2, a mesoporous silica matrix remains after the template is removed by calcination. The remaining materials has a high surface area of roughly 1000 m^2/g and pores in the order of 2 nm. The material is commonly characterized using nitrogen adsorption isotherms, which allows the determination of surface area, pore size and pore volume[26]. Nitrogen adsorption isotherms are discussed in more detail in section 2.4.1.

2.2.3. Template removal

Removal of the porosity template can be achieved via three methods; calcination[24], ion-exchange[27], and sonication assisted dissolution[28]. While all three methods remove the porosity template from the silica, calcination has the added effect of increasing the silica condensation[16]. If the MCM-41 silica is grown around a shape template, a template removal method can be chosen that either retains or removes the shape template material. Sonication aided dissolution has little effect on the cuprous oxide template, but ion-exchange and calcination have significant effect on the core composition. The three template removal techniques are discussed in more detail on the following page.

Calcination

Calcination is generally done by heating the sample to circa 500 °C in air for several hours, burning off any organic material. Since calcination is a dry treatment, it can be difficult to disperse the nanoparticles afterwards[16]. To ensure particles can be dispersed after calcination, the calcination can be performed in a high boiling point liquid such as TOPO (BP = 411 °C) or squalene (BP = 275 °C). Although in-liquid calcination cannot provide equally high temperatures as traditional calcination, the temperature seems high enough to remove CTAB, as similar MCM-41 surface areas are reached as with dry calcination[16]. In liquid calcination can significantly affect the cuprous oxide template, which will be discussed in section 2.3.3.

Ion-exchange

Ion-exchange is based on the exchange of CTA^+ ions from the porosity template with ions in solution. Ammonium salts proved most effective in the extraction of MCM-41, after comparing ion exchange extracted MCM-41 with calcinated MCM-41[27]. Boiling MCM-41 in an ethanolic ammonium chloride solution for 60 minutes removes 75% of the CTAB template[27]. Since ethanolic ammonium chloride dissolves cuprous oxide, this method also removes the shape template.

Sonication assisted dissolution

Jabariyan *et al.* investigated the removal of CTAB from MCM-41 by disrupting the micellar template with ultrasound the presence of alcohol. A single, 15 minute, sonication step removes 93% of the CTAB template, and subsequent sonication steps remove residual CTAB and increased sample surface area[28]. Depending on the required effect on the cuprous oxide template, a suitable extraction method can be chosen.

2.2.4. Silica modification

Since the colloidal properties are largely dependent on the surface of the nanoparticle, a surface modification can be applied to influence stability. Stöber silica is normally hydrophilic, with its negatively charged surface stabilizing the colloids in polar solvents. If hydrophobic groups are attached to the surface, the colloidal dispersion can become more stable in a-polar solvents[29]. An example is the treatment with trimethylsilanol[30]. In this treatment, the residual hydroxyl groups on the surface of the silica condensate with the hydroxyl group of trimethylsilanol, resulting in silica with a methylated surface. The product formation is promoted by using a high concentration of trimethylsilanol and elevating the temperature to 110 °C to remove produced water. Trimethyl siloxane can also be attached to the surface using hexamethyldisilazane under an N_2 atmosphere[30].

2.3. Functional nanoboxes

In addition to providing extra control over the refractive index, the internal void and the porosity of the cube provide a novel opportunity to add functionality to ARCs. One example is incorporation of nanoparticles in the void. A simple example of nanocube functionalization would be the incorporation of anti-fouling materials. Silver nanoparticles encapsulated in silica are known to have high anti-bacterial activity[31]. Another example can be found in silica encapsulated gold nanoparticles, which are known to photocatalyse the degradation of organic molecules[32]. Functional nanoboxes might find application in fields were cubic colloids are already being used. This design provides additional functionality, without changing the colloidal properties of the system.

A problem with deposition of functional materials inside hollow nanoparticles is selective deposition in the particle void. Non-specific, random nucleation results in a low fraction of particles within the particle void. Two approaches are possible to circumvent this non-specific deposition problem. The former approach to solving this problem is nucleating a large amount of seeds followed by only growing the seeds nucleated in a nanobox. The latter approach makes use of the cuprous oxide shape template inside the nanobox, transforming it into the required functional material. Since both approaches have their advantages and limitations the suitability of either approach depends on the desired functionality.

2.3.1. Deposition by seeded growth

Gold nanoparticles can be grown inside hollow silica nanoparticles via a seeded growth technique[14]. By nucleating a large amount of gold seeds in a dispersion containing hollow silica nanoparticles, some nucleating takes place in the hollow silica particles. The silica nanoparticles, and their incorporated seeds, are separated from the seed dispersion and added to a growth solution. In this solution the gold seeds are grown into larger nanoparticles. Xiao *et al.* used this method to fill large silica spheres with gold nanoparticles as depicted in Figure 3, Left[14].

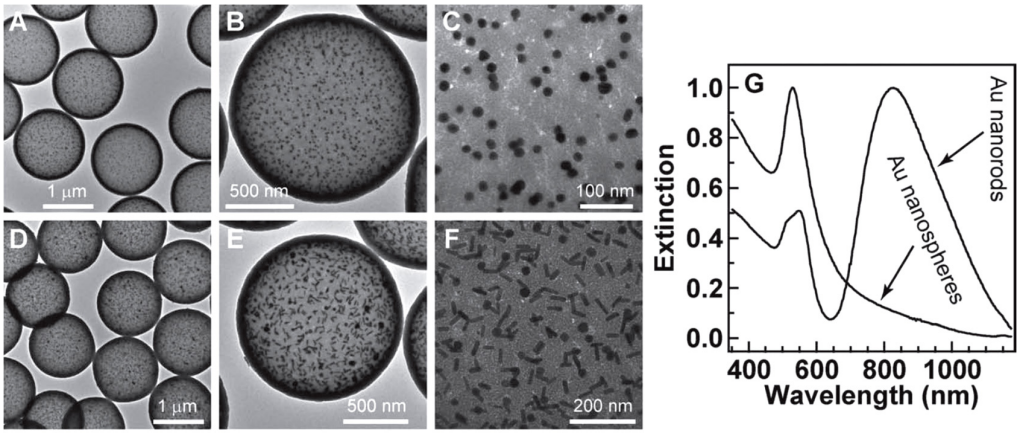

*Figure 3: **A-C:** Gold nanospheres and **D-F:** nanorods incorporated in hollow silica spheres. **G:** UV-Vis spectrum of particle dispersions.*[14]

Xiao *et al.* concluded the deposition of gold particles was successful via TEM, and UV-Vis, where the surface plasmon resonance of the gold particles is visible (Figure 3: Right). However, it is difficult to assess whether the gold nanoparticles are free inside the void or stuck in or on the silica shell. The increased gold nanoparticle concentration towards the edge of the silica edge visible on the TEM images, suggests the particles are stuck to the silica wall. The seeded growth technique is not limited to gold nanoparticles. In principle, if nanoparticles can be produced via a bottom-up approach, they can be deposited into hollow silica nanoparticles. One example is the deposition of quantum dots inside hollow porous silica nanoparticles. The functionalization of nanoparticles for antireflective coatings with quantum dots would be extremely interesting for photovoltaic applications. The ability to incorporate up-, or down-converting quantum dots into anti-reflective coatings could significantly improve cell efficiency by converting light that is ordinarily not converted by the photovoltaic cell. While up-conversion is already being used by the photovoltaic industry, the incorporation into the anti-reflective coatings could increase efficiency and reduce production costs.

2.3.2. Template disproportionation

A large challenge of the seeded growth technique is the consistent filling of all hollow silica nanoboxes[33]. This challenge is overcome by using the material already present in the void. By transforming the cuprous oxide, all nanocubes can be filled with a consistent amount of functional material, creating a well-defined system. Jiang *et al* used this method to transform the cuprous oxide core inside a silica shell into a metallic copper core[34]. Here the transformation is based on the ability for dissolved Cu^+ to disproportionate to metallic copper and Cu^{2+} (reaction 3). Jiang *et al.* made use of sulfuric acid to dissolve the cuprous oxide, followed by disproportionation of the Cu^+ ions inside the shell.

$$2\,Cu^+ \rightarrow Cu + Cu^{2+} \qquad (reaction\ 3)$$

Since Cu^+, Cu^{2+} and H^+ ions are all able to diffuse through the 0.3 nm pores of Stöber silica, the dissolved copper ions can also leave the shell before disproportionation. For the metallic copper particle to nucleate inside the silica shell, it is important that the disproportionation largely occurs Inside the silica shell.

2.3.3. Template thermolysis

Another way to transform the cuprous oxide shape template into a metallic copper core is by expulsion of oxygen from the cuprous oxide. Upon heating of cuprous oxide over 310 °C under a N_2 atmosphere, the oxygen diffuses out, leaving metallic copper behind (Figure 4)[35]. As discussed in section 2.2.3 on MCM-41 calcination, in liquid calcination is preferred to dry calcination. As such it is likely that in liquid thermolysis is preferred to dry thermolysis. Since TOPO has a boiling point above the temperature required for thermolysis, it can likely be used for in liquid thermolysis.

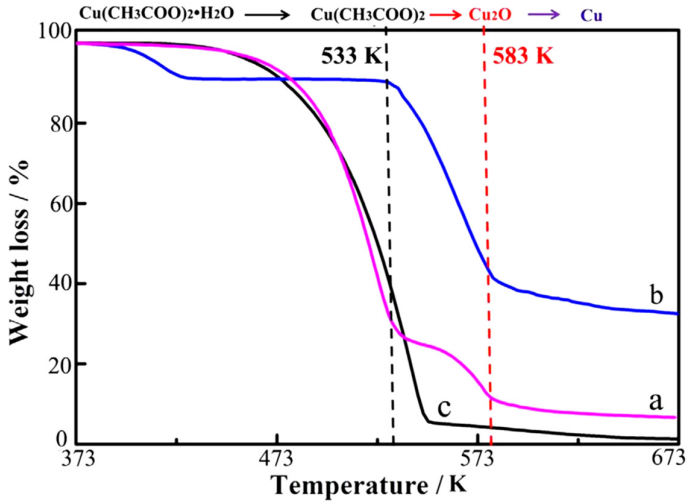

Figure 4: Thermogravimetric analysis detailing cuprous oxide thermolysis in nitrogen atmosphere[35].

After the oxygen is removed from the cuprous oxide matrix, a copper structure remains, which reforms to a copper core at high temperatures. For metallic colloids, this restructuring is likely influenced by size dependent melting effects[36]. Yeshchenko *et al.* investigated the influence of the copper nanoparticle size on the melting temperature, and concluded that the temperatures are significantly lower for particles below 100 nm[36]. The lower melting temperatures are attributed to the higher surface to volume ratio, increasing the effect of surface diffusion. As shown in Figure 5, for particles below 50 nm, the melting temperatures become within the range of in-liquid thermolysis temperatures.

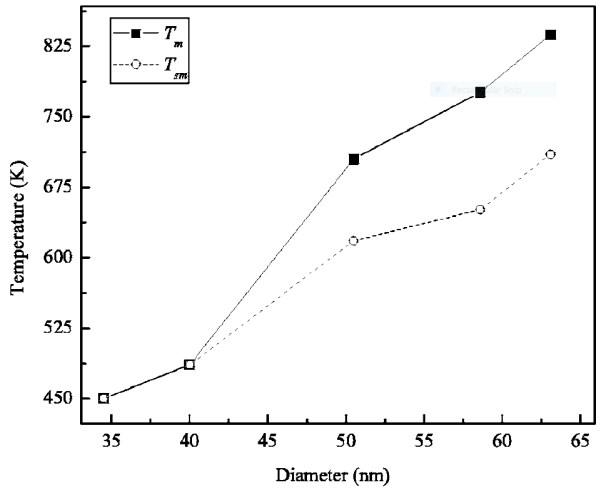

Figure 5: Melting point (closed square) and surface melting point (open circle) of colloidal copper[36].

2.3.4. Galvanic displacement

In the field of electrocatalysis, galvanic displacement is a widely used technique in the wet synthesis of catalysts[37]. The technique enables the exchange of a less-noble metal with more noble metals. For example, a silver template can perform a redox exchange with Pt^{2+} ions, following the redox reaction displayed in Table 1.

Table 1: Redox (half)reactions for silver-platina displacement with standard potential.

Reaction	Standard potential (V)
$\boldsymbol{2\,Ag(s) \rightarrow 2\,Ag^{+}(aq) + 2\,e^{-}}$	- 0.80
$\boldsymbol{Pt^{2+}(aq) + 2e^{-} \rightarrow Pt(s)}$	+ 1.18
$\boldsymbol{2\,Ag(s) + Pt^{2+}(aq) \rightarrow Pt(s) + 2\,Ag^{+}(aq)}$	+ 0.38

As long as the desired metal has a higher reduction potential, galvanic displacement can be performed to transform the template. In Table 2, the reduction potentials of several common metals are set out. The top five, gold, platina, palladium, silver and ruthenium, are suitable for the galvanic displacement of copper. The bottom two, nickel and cobalt, are less noble than copper, and can not be used for the galvanic displacement of copper.

Table 2: Metal ion reduction half reactions ordered by standard potential.

Reaction	Standard potential (V)
$Au^{3+}(aq) + 3\,e^- \rightarrow Au(s)$	+ 1.50
$Pt^{2+}(aq) + 2\,e^- \rightarrow Pt(s)$	+ 1.18
$Pd^{2+}(aq) + 2\,e^- \rightarrow Pd(s)$	+ 0.95
$Ag^{+}(aq) + e^- \rightarrow Ag(s)$	+ 0.80
$Ru^{2+}(aq) + 2\,e^- \rightarrow Ru(s)$	+ 0.45
$Cu^{2+}(aq) + 2\,e^- \rightarrow Cu(s)$	**+ 0.34**
$Ni^{2+}(aq) + 2\,e^- \rightarrow Ni(s)$	- 0.26
$Co^{2+}(aq) + 2\,e^- \rightarrow Co(s)$	- 0.28

Since galvanic displacement occurs on the metal surface, the effectivity is highly dependent on the diffusion of the less noble metal inside the newly created noble metal shell[38]. During the first phase of complete displacement, the first noble ions displace the outer most template atoms, creating a shell of noble metal around the template. After the shell formation, galvanic displacement effectivity is highly dependent upon the diffusivity of template atoms through the noble metal shell. If this diffusivity is too low, displacement cannot continue since the noble shell protects the template. For most metals, however, the diffusivity is significant, and the template can diffuse through the noble shell and reach the surface to be displaced by noble metal ions. Additionally, the concentration of noble metals influence the final product. If the noble metal ions are added in excess, the template is completely displaced, otherwise, a core-shell structure is formed.

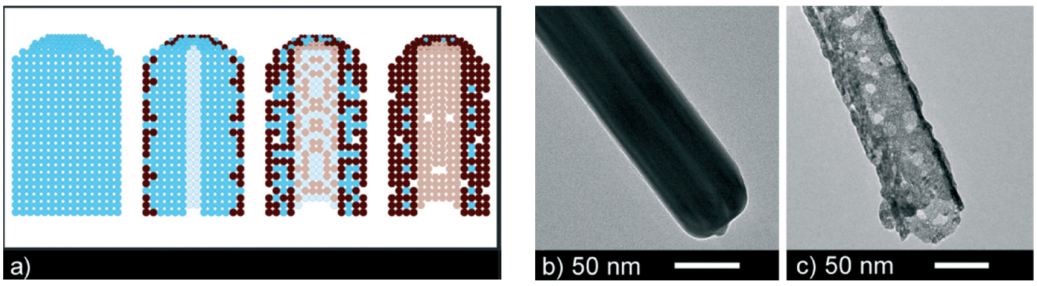

*Figure 6: A: Graphical representation and TEM images **B**: before and **C**: after Ag-Pt galvanic displacement[37].*

Complex structures can be formed during galvanic displacement. The formation of these structures is described by the Kirkendall effect[39], of which the hollow tubes formed by silver-platinum displacement, visible in Figure 6, are an example. The effect stems from the higher diffusivity of template metals in the noble metal, than the noble metal in the template. In Figure 7 the displacement of silver by gold, on a SiN_x substrate, is schematically displayed. After a gold shell is formed, the displacement continues through the diffusion of silver through the golden shell. As a consequence, the core is leached out and a void is formed[39].

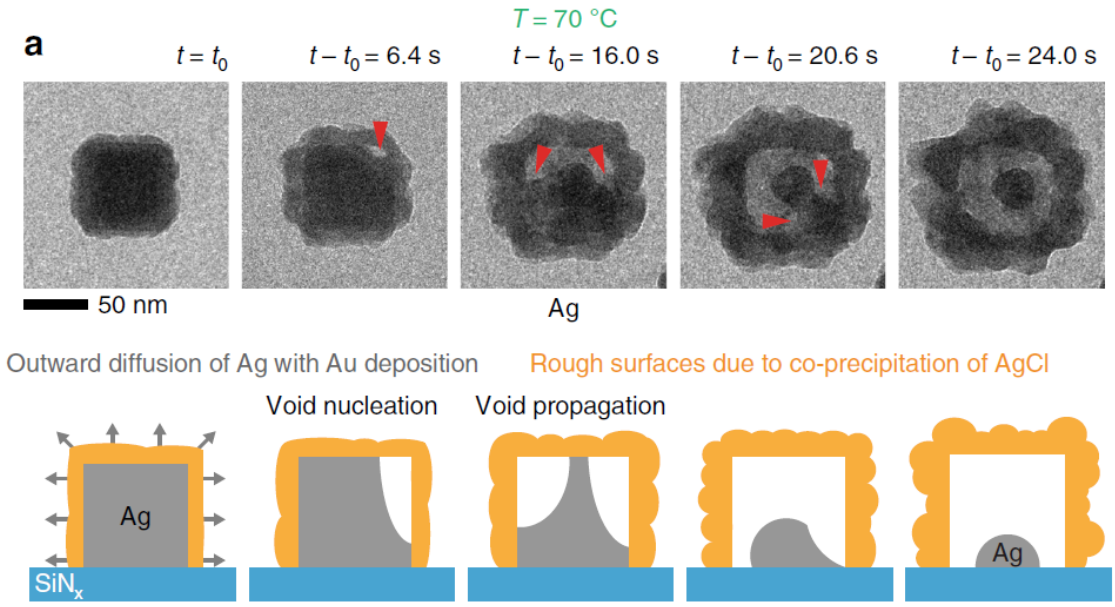

Figure 7: TEM images and Graphical representation of Ag-Au galvanic displacement[39].

Since galvanic displacement allows the wet synthesis of complex, high surface area, noble metal nanoparticles, the technique is widely used in the production of catalysts. An example of such a catalyst is the Ni@Pt particle depicted in Figure 8, which exhibit high activity per gram of platina[37]. Since metals and alloys are not distinguishable on TEM imaging, an extra technique is necessary to determine if the content of the highly scattering material seen on TEM consists of the shape template metal, the noble metal or a combination. Energy-dispersive X-ray spectroscopy (EDX) mapping is an excellent technique to gather such specific information. EDX is further discussed in 2.4.2.

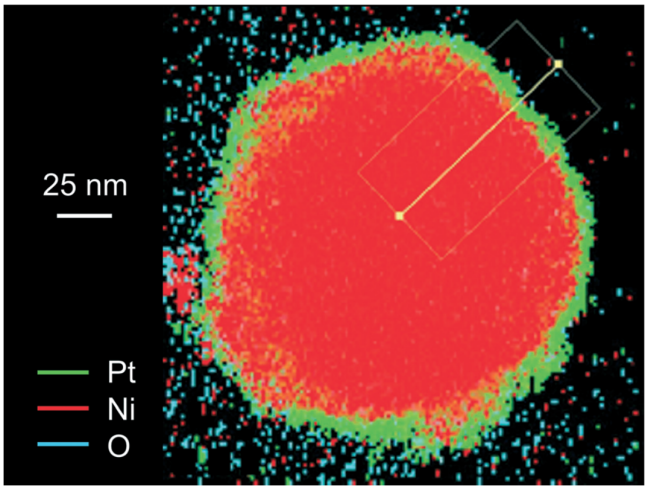

Figure 8: EDX map of Ni@Pt particle produced using galvanic displacement[37].

2.4. Characterization Methods

2.4.1. Nitrogen physisorption

Nitrogen physisorption is widely used to determine the pore size and surface area of porous materials. During a physisorption measurement, the sample is placed in a high vacuum chamber at the boiling point of the probing medium, which is 77 K for nitrogen physisorption. Measured amounts of nitrogen gas are then introduced into the chamber and the resulting chamber pressure is measured. The physisorption of nitrogen onto the sample surface results in a non-linear pressure increase . The resulting P/V isotherm reflects how the nitrogen adsorbs onto sample surface and fills the sample pores. Once the chamber approaches P_0, the boiling pressure for nitrogen at 77 K, the measurement is reversed and hysteresis caused by capillary effects can be detected.

In 1937, Brunauer, Emmett and Teller published an approach to derive the surface area from the isotherm[40]. The approach is an extention of the Langmuir adsorption model and as such assumes ideal gas behavior. Additionally the approach assumes simplified behavior of adsorbed nitrogen layers, gas molecules only interacting with adjacent molecules, the enthalpy of adsorption of the first layer greater than the second layer, and the second and following layers have an equal enthalpy of adsorption. With these simplifications the adsorption of nitrogen onto a substrate is truly random adsorption, with a preference for the first nitrogen layer. These assumptions allow the derivation of the BET equation,

$$\frac{p}{v(p_0 - p)} = \frac{1}{v_m c} + \frac{c-1}{v_m c}\frac{p}{p_0}. \tag{6}$$

Plotting the sample isotherm $p/v(p_0-p)$ against p/p_0 results in a straight line at low p, with an intercept of $1/v_m c$ and a slope of $(c-1)/v_m c$. Subsequently, from the slope and intercept, the v_m (volume of the nitrogen monolayer) and c (the BET constant) can be determined. Combined with the sample weight, the surface area per gram is calculated.

In 1951, Barrett, Joyner and Halenda published an approach to derive the pore volume of porous materials from the nitrogen isotherm[41]. The approach is based on the combination of the BET approach and capillary condensation. In addition the assumptions of the BET approach, the BJH approach assumes open, cylindrical pores. The deviation from the isotherm of a nonporous material, caused by capillary condensation, in combination with the Kelvin equation, is used to determine the pore volume of the sample.

Figure 9 displays a typical MCM-41 isotherm[42]. Analysis of the isotherm data provides estimates of the sample surface area and pore size distribution. For commercial MCM-41 the surface area is circa 1000 m^2/g, and the pores have a diameter between 2 and 3 nm[43].

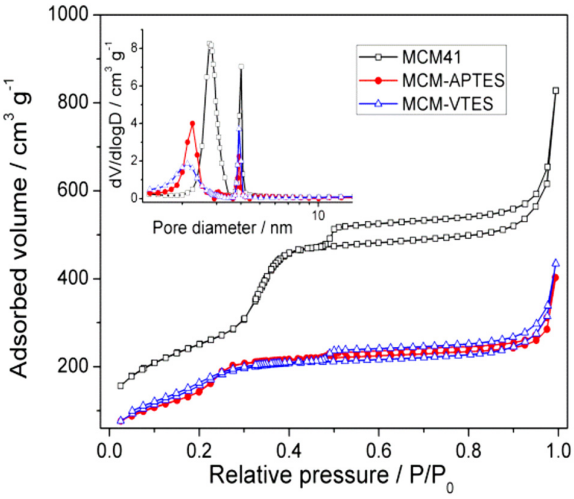

*Figure 9: Main: Nitrogen physisorption isotherm of MCM-41 (white-open) and modified MCM-41 (closed-red and open-blue) with **Inset**: BJH pore size distribution[42].*

2.4.2. Energy-dispersive X-ray spectroscopy

EDX is an elemental analysis technique which, in combination with TEM, is able to determine the elemental composition of a sample. When an inner shell electron is ejected by a high energy electron beam, a higher shell electron can fill this hole upon emission of a photon. The energy of this photon is dependent on the energy difference between the ejected electron, and the electron filling the hole. Due to the unique nature of each element, this photon energy is element specific. After detection, the energy of the photon is compared to known values to determine the element of origin. The sample can be scanned with the high energy beam to determine the elemental composition at each position. Combined with STEM, elemental maps can be used to determine the elemental composition of a nanoparticle. For example, the EDX mapping in Figure 10 reveals that for the depicted Cu/Pt/Au particle, the core is a mixed alloy, while the surface is predominantly platina. This information could not have been gathered with TEM alone and is vital for monitoring the galvanic displacement of nanoparticles.

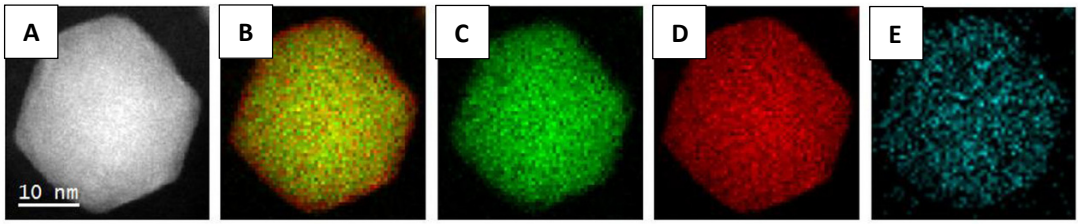

*Figure 10: ADF (**A**) and EDX maps, Cu (**C**), Pt (**D**) and Au (**E**) nanoparticle. Note the red platina edge on the overlay map (**B**)[44].*

2.4.3. Catalytic degradation

The catalytic degradation of dye molecules is a technique commonly used to determine the catalytic effectivity of metal colloids. The degradation of dyes can be easily evaluated visibly qualitatively, or with UV-Vis spectrophotometry for quantitative analysis. A suitable reaction has to be chosen depending on the catalyst. Since the degradation of organic dye molecules by sodium borohydride is commonly catalyzed by metal surfaces, it can be used as a benchmark for catalytic activity. Congo red is such an organic dye[45]. Since the degradation is kinetically unfavorable, the reaction is slow without catalyst. As the reaction progresses, Congo red is degraded into biphenyl and sodium 4-amino-1-

naphthalene sulfonate (Figure 11)[46]. Both products have no significant absorption of visible light, resulting in a transparent solution. The reaction can be followed over time using UV-Vis spectrophotometric analysis to determine the reaction rates.

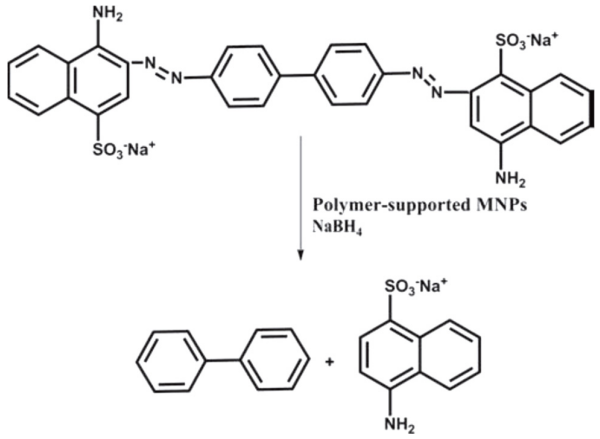

Figure 11: Congo red degradation reaction[46].

Plotting the catalytic degradation rate against the dye concentration can then provide insight in the into the reaction order with respect to the dye concentration. Generally, for bimolecular surface reactions two main reaction mechanisms are known, Langmuir–Hinshelwood mechanism, and the Eley–Rideal mechanism[47,48].

Langmuir–Hinshelwood[49]

For the Langmuir–Hinshelwood mechanism, both reactant molecules A and B are adsorbed on the surface. With increasing concentrations of either A or B the reaction rate increases, the reaction is thus first order in both reactants. Once the surface becomes saturated with A and B, the rate become independent of their solution concentrations, the reaction order is now zero with respect to A and B, and the reaction rate is dependent on the surface reaction rate and the product desorption. If the surface becomes dominated by either of the reactants, the reaction cannot take place quickly and the rate declines. In this situation, the reaction is order becomes minus one for the domination reactant.

Eley–Rideal mechanism[48]

For the Eley–Rideal mechanism, only one of the reactants is adsorbed onto the surface, with the second reactant reacting directly from the solution. With increasing concentration of the adsorbed (A) and dissolved (B) reactant, the reaction rate increases and the order is one with respect to both reactants. Once A saturates the surface, and B is available in excess, the reaction rate becomes independent of their solution concentrations, the reaction order is zero with respect to A and B. The reaction rate is now dependent on the surface reaction rate and the product desorption rate.

Using this insight into the reaction mechanisms, in combination with the reaction rate - reactant concentration plot, the maximum catalytic rate and the reaction order can be derived.

3. Materials and methods

3.1. Materials

Chemical	Abbreviation	Source	Grade
1,5-pentanediol		Sigma-Aldrich	≥97%
1-Ocatadecene		Aldrich	90% techn.
Acetone			Technical
Ammonium chloride		Sigma-Aldrich	≥99.5%
Congo red		Aldrich	91 wt.% dye
Copper (II) acetylacetonate	$Cu(acac)_2$	Aldrich	≥97%
Ethanol		VWR	Absolute/Technical
Gold(III) chloride trihydrate	$HAuCl_4$	Aldrich	99.9%
Cetyl trimethylammonium bromide	CTAB	Acros Organics	≥99%
Hexamethyldisilazane	HMDS	Aldrich	99.9% Reagentplus
Hydrochloric acid		Acros Organics	37% aq.)
L-Ascorbic acid		Sigma	reagent grade
Methyl isobutyl ketone	MIBK	Scharlau	ACS reagent grade
Methylene blue		J.T.Baker	Baker grade
n-Hexane		EMSURE	ACS reagent
Nitric acid		Emsure	65% aq.
Polyvinylpyrrolidone 40kg/mol	PVP-40	Sigma-Aldrich	
Polyvinylpyrrolidone 55kg/mol	PVP-55	Aldrich	
Potassium Bromide	KBr	Acros organics	≥99% IR grade
Rhodamine B		Sigma	≥95%
silver nitrate		Sigma-Aldrich	99%
Sodium borohydride		Sigma-Aldrich	≥98.5%
Sodium hydroxide		Merck	≥99%
Sulfuric acid		Fischer	95% aq.
Tetraethylorthosilicate	TEOS	Aldrich	≥99.0%
Trimethyl ammonium hydroxide	TMAH	Sigma-Aldrich	25% wt aq.
Trimethylsilanol	TMS	Aldrich	≥98.5%
Trioctylphosphine oxide	TOPO	Aldrich	99%

All chemicals were used as obtained. All used water was obtained from a Synergy Millipore filter system (18.2 MΩcm at 20 °C).

3.2. Porous nanoboxes

3.2.1. Synthesis of Cu_2O Cubes

Two batches (AS1-61 and AS1-63) of Cu_2O cubes were produced during the course of this project using a modified procedure from Dekker *et al.*[13]. A typical synthesis was as the following. To a 500 mL 3-neck round-bottom flask equipped with reflux and dripping funnel, 223 g 1,5-pentanediol and 25.3 g PVP-55 were added. The reflux condenser and dripping funnel were connected to a N_2/Vacuum Schlenk line. The mixture was flushed three times at room temperature, heated to 100 °C by oil bath and flushed three times. 5.2 g $Cu(acac)_2$ and 75 g 1,5-pentanediol were weighed in a 100 ml bottle and mixed by a combination of shaking and sonication. The $Cu(acac)_2$ mixture was transferred to the

dripping funnel and flushed four times. The PVP-55 solution was heated to 200 °C and the $Cu(acac)_2$ mixture was added over 30 seconds with N_2 pressure. The reaction mixture temperature dropped to 170 °C and subsequently slowly increased back to 200 °C during the reaction. After 22 minutes, heating was discontinued, and the mixture was allowed to cool down, yielding a brown mixture. The product was collected with 500 ml acetone. The resulting sol was separated by centrifugation (3000g 2.5 hours) and washed twice with ethanol by centrifugation (12000 g, 30 minutes). Finally, the sample was dispersed in 50 mL ethanol.

3.2.2. Porous silica coating

The coating of cuprous oxide nanocubes was attempted via three methods, A, B and C. The procedures were adapted from A; Kato *et al.*[11], B; Kato *et al.*[7] combined with Jiang *et al.*[34], and C; Jiang *et al.*[34]. The differences between procedures are separately described below. Differences reside in addition sequence and the base catalyst used.

A

Synthesis was carried out in a 500 mL 2-neck round-bottom flask, half submerged in a sonication bath and equipped with a mechanical stirrer. 200 mL ethanol and 100 mL water were added. 100 mg cuprous oxide nanocubes, TMAH (6 mL 1%wt. aqueous solution) and 0.2 g CTAB was added. Sonication and stirring was started and after 15 minutes 300 µL TEOS was added with a Gilson peristaltic pump over 45 minutes. For all three synthesis procedures the sonication was continued for at least 2 hours after addition of the reagents. Stirring was continued overnight. The sol was washed trice with ethanol by centrifugation (12000 g, 30 minutes) and dispersed in 5 ml ethanol.

B

Synthesis procedure was carried out in a 500 mL 2-neck round-bottom flask, half submerged in a sonication bath and equipped with a mechanical stirrer. 200 mL ethanol and 100 mL water were added. 100 mg cuprous oxide nanocubes, 2 mL 0.1M sodium hydroxide and 0.2 g CTAB was added. Sonication and stirring was started and after 15 minutes 300 µL TEOS was added with a Gilson peristaltic pump over 45 minutes. Sonication was continued for at least 2 hours after addition of the reagents. Stirring was continued overnight. The sol was washed trice with ethanol by centrifugation (12000 g, 30 minutes) and dispersed in 5 ml ethanol.

C

Synthesis procedure was carried out in a 500 mL 2-neck round-bottom flask, half submerged in a sonication bath and equipped with a mechanical stirrer. 36 mL water, with ethanol added to a total volume of 200 mL, were added. 100 mg cuprous oxide nanocubes, 125 µL TEOS and 0.2 g CTAB was added. Sonication and stirring was started and after 15 minutes 10 mL 20 mM sodium hydroxide was added with a Gilson peristaltic pump over 10 minutes. Sonication was continued for at least 2 hours after addition of the reagents. Stirring was continued overnight. The sol was washed trice with ethanol by centrifugation (12000 g, 30 minutes) and dispersed in 5 ml ethanol.

3.2.3. Template removal

The following ion exchange template removal procedure was used to remove the CTAB and Cu_2O template, adapted from Deekamwong *et al.*[27]. To a 100 mL 2-neck round-bottom flask equipped with magnetic stirring and a reflux condenser, 2.5 mL silica coated cubes (50 mg Cu_2O) and 33 mL ethanol were added. Ammonium chloride (1.02 g) was added and the mixture was refluxed for 45 minutes. Heating was removed and the mixture was allowed to cool down, yielding an aqua mixture. 33 mL water followed by a drop a nitric acid were added, yielding a clear liquid. The product was washed by centrifugation and dispersed in 80 mL water. The product was washed with water twice, and ethanol thrice, by centrifugation (20000 g, 40 minutes). The product was dispersed in 5 ml ethanol.

3.2.4. Hydrophobic surface modification Trimethylsilanol

$Cu_2O@SiO_2$ (10 mg dry weight in 0.5 mL ethanol) was added to ethanol (0.5 mL) in a 20 mL sample vial. TMS (1 mL) was added and the sample vial was heated to 110 °C using an oil bath. After a 90 minutes heating period, the mixture was removed from the oil bath. Ethanol (30 mL) was added and the dispersion was washed with ethanol (twice), hexane (twice) and octadecene (twice), by centrifugation (3000 g, 2 hours). The sample was finally dispersed in 10 mL octadecene.

3.2.5. Hydrophobic surface modification Hexamethyldisilazane

$Cu_2O@SiO_2$ (10 mg dry weight in 0.5 mL ethanol) was separated by centrifugation and dispersed in MIBK 1 mL. The dispersion was added to a reaction tube and heated to 50 °C while stirring under N_2. Under N_2 atmosphere, 2 mL HMDS was added and the reaction was allowed to continue for 20 hours. Stirring, heating and N_2 were then removed and the dispersion was washed with ethanol (twice), and octadecene (twice), by centrifugation (3000 g, 2 hours). The product was finally dispersed in 10 mL octadecene.

3.3. Functional nanoboxes

3.3.1. Gold seeded growth

Hollow nanoboxes were filled with gold particles using a seeded growth approach adapted from Xiao *et al.*[14]. 5 mL porous hollow nanoboxes (preparation described in section 3.2.3) were dispersed in CTAB (9.75 mL 0.1 M) and $HAuCl_4$ (0.25 mL 10 mM) in a 20 mL sample vial. The mixture was sonicated for 15 minutes, after which $NaBH_4$ (0.6 mL 10 mM) was added under stirring. The sample was left for 2 hours and washed with CTAB (0.1 M) by centrifugation twice and dispersed in 5 mL water.

A growth solution was prepared with $HAuCl_4$ (0.25 mL 10 mM), CTAB (10 mL 0.1 M), hydrochloric acid (0.2 mL 1 M) and Ascorbic acid (0.04 mL 0.1 M). The seed solution (100 µL) was added and the mixture was left overnight. The dispersion was washed with CTAB (0.1 M) (once) and water (twice) by centrifugation. The product was dispersed in 1 ml ethanol.

3.3.2. Quantum dot deposition

Oleic acid (12 mL) and Octadecene (34mL) were added to a 100 mL 3-neck round-bottom flask equipped with magnetic stirring, a thermometer, a Vigreux condensator and a N_2/Vacuum Schlenk line. Erbium acetate (13.8 mg), Yttrium acetate (425.5 mg) and Ytterbium acetate (126.4 mg) were added and the mixture was degassed at 120 °C for 30 minutes. Hollow hydrophobic cubes (1mL, 25 mg start core equivalent) in octadecene were added and the mixture was degassed for 60 minutes. Methanol (20 mL containing 200 mg sodium hydroxide and 296.9 mg ammonium fluoride) was transferred to the reaction vessel under N_2 flow. The temperature was raised to 60 °C and vacuum was applied until most methanol was removed. The mixture was flushed thrice at 120 °C to remove residual methanol and the temperature was raised to 300 °C in 30 minutes. After 2 hours, heating was stopped and the temperature was reduced to room temperature using a water bath. Ethanol (46 mL) was added and the sample was separated by centrifugation (2000 rpm 8 minutes). The sample was washed twice by dispersing the sediment in 10 mL cyclohexane, adding 10 mL ethanol and separating by centrifugation (2000 rpm, 8 minutes). The sediment was dispersed in two volumes of 5 mL cyclohexane.

3.3.3. Cu_2O disproportionation with H_2SO_4

$Cu_2O@SiO_2$ (30 mg dry weight in 1.5 mL ethanol) was separated by centrifugation and dispersed in 10 mL water. The dispersion was added to sulfuric acid (50 mL 0.36 M), left undisturbed for 30 minutes and washed with water (twice) and ethanol (twice) by centrifugation and finally dispersed in 5 mL ethanol.

3.3.4. Air calcination

All dispersions were dried in porcelain bowls for 30 minutes circa 30 cm under a 150 W lamp. The samples were heated in a Nabertherm P330 oven with a ramp of 106 °C/min up to 500 °C. Temperature was kept at 500 °C for 5 hours after which the oven was allowed to cool down overnight. Ethanol (2 mL) was added and the samples were dispersed by scraping the dried particles and sonication.

3.3.5. In liquid calcination

TOPO (7.1 g) was transferred into a 100 ml 2-neck round-bottom flask equipped with a reflux condenser, stirrer and a N_2/Vacuum Schlenk line. The TOPO was heated to 60 °C and $Cu_2O@SiO_2$ (50 mg dry weight in 2.5 mL ethanol) was added. The ethanol was removed from the mixture by applying vacuum after which and the mixture was heated to 350 °C under N_2 flow. After one hour at 350 °C, heating was stopped and the mixture was allowed to cool down to 100 °C. Samples were taken and quenched in ethanol before, during and after the heating process. Water (25 mL) was added and the sample was washed with water (thrice) and ethanol (thrice) by centrifugation. Finally, the product was dispersed in ethanol (50 ml).

3.3.6. Galvanic displacement with ascorbic acid pretreatment

The copper core inside a porous silica shell was exchanged with silver via the following procedure adapted from Stewart *et al.*[50]. $Cu@SiO_2$ (0.4 mg in 1 mL ethanol) was separated by centrifugation(16000 g, 10 minutes) and dispersed in water (0.5 mL). Freshly prepared ascorbic acid (0.5 mL 1.16 M) was added and the mixture was vortexed for 10 seconds. The mixture was directly washed with water twice by centrifugation and dispersed in water (0.5 mL). silver nitrate (0.5 mL 50mM) was added and the mixture was vortexed for 10 seconds. The mixture was directly washed with water (twice) and ethanol (twice) by centrifugation and dispersed in 5 mL ethanol.

For galvanic displacement with gold, 0.5 mL $HAuCl_4$ 25 mM was used instead of 0.5 mL silver nitrate 50 mM.

3.3.7. Catalysis measurements.

The catalytic activity silica nanocubes containing a silver core was determined by degradation of congo red dye. The nanoparticle dispersion (1ml dispersion produced in 3.3.6) of the sample cubes was separated by centrifuge and dispersed in water (1 mL). Three 20 mL sample vials, labeled C (catalyst), E (empty) and R (reference) were filled according to Table 3.

Table 3: catalytic activity check vial composition.

Vial	Water	Dye (20mM)	Nanoparticles
R	10 mL	50 µL	-
E	9 mL	50 µL	$Void@SiO_2$ (1 mL)
C	9 mL	50 µL	$Metal@SiO_2$ (1 mL)

Freshly prepared sodium borohydride (0.5 mL, 1M) was added to each vial and changes in color were observed visually.

3.3.8. Ag@SiO2 Congo Red degradation rate

$Ag@SiO_2$ (0.5 ml dispersion produced in 3.3.6) was separated by centrifugation and dispersed in water (1 mL). Two sample vials were labeled with D (Dye) and R (Reference) and were filled according to Table 4.

Table 4: Degradation rate vial composition.

Vial	Water	Dye (20mM)	Nanoparticles
D	9 mL	50 µL	$Ag@SiO_2$ (0.5 mL)
R	9 mL	-	$Ag@SiO_2$ (0.5 mL)

Freshly prepared sodium borohydride (0.5 mL, 1M) was added to each vial and a timer was started. The reaction was monitored by UV-Vis.

Over time several UV-Vis spectra were collected. For each measurement, 2 mL of each sample was transferred to a quartz cuvette. A spectrum was collected of the Dye cuvette with the Reference cuvette in place. The time at the start of the measurement was noted. The cuvettes were removed from the spectrophotometer and the sample liquid was returned to the sample vials.

3.4. Characterization

The solid content of the samples was determined by drying a known volume of dispersion on an aluminum dish under a 150 W lamp and weighing the residue.

For IR spectra collection, 250 mg KBr with 1 mg sample was dried in a Memmert oven at 70 °C overnight, copper core samples were dried under vacuum and nitrogen flow. Of the sample a KBr matrix was pressed and the spectrum was recorded from 400-4000 cm^{-1} on a PerkinElmer FT-IR/FIR Frontier spectrometer. IR spectra were normalized to the strongest peak, excluding the O-H stretch peak if present.

TEM samples were prepared by diluting part of the sample in water and drying a droplet on a Cu/Polymer grid under a 150 W lamp. The colloids were imaged using a Phillips Tecnai 12 and 20 operating at 120 and 200 kV. Images of nanoparticles were analyzed with ImageJ, conducting at least 100 measurements per sample.

EDX mapping was conducted on a FEI Talos F200X, with samples prepared on an aluminum/polymer grid.

For adsorption Isotherm measurement, the samples were dried overnight at 250 °C under a nitrogen atmosphere. Measurements were performed on a Micrometrics TriStar II Plus.

UV-Vis spectra were collected using a PerkinElmer Lambda 35 UV/VIS spectrometer in combination with quartz cuvettes. UV-Vis spectra were normalized to the strongest peak.

A noble metal acid test was performed by adding nanoparticles dispersed in water to 0.5 mL concentrated nitric acid. Effect of the nitric acid was observed visually and via TEM imaging.

4. Results and discussion

4.1. Porous nanoboxes

4.1.1. Synthesis of Cu_2O cubes

The first step of the nanobox synthesis was the preparation of the cubic cuprous oxide template. The synthesis produced two batches with solid contents of 1.182 and 0.808 g, corresponding to a copper conversion of 83.4 and 56.4%. As visible in the TEM images in Figure 12, the synthesis resulted in highly cubical nanoparticles.

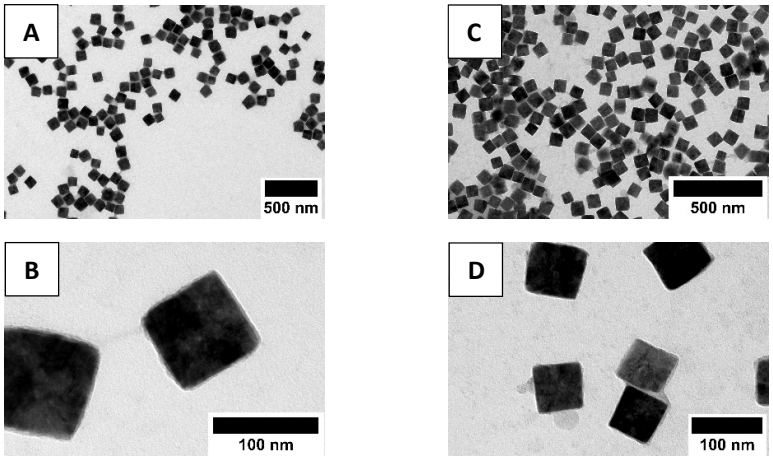

*Figure 12: **A-B**: Batch 1. **C-D**: Batch 2.*

The edge-length of the obtained particles was obtained by manually analyzing the TEM images in ImageJ, The averages and standard deviations are presented in Table 5. The strong Cu-O absorption at 630 cm^{-1} in the IR spectrum (Figure 13) confirms that the formed nanoparticles are indeed Cu_2O.

Table 5 Cuprous oxide cube parameters measured from TEM images.

Batch	Edge length
1	96 ± 10 nm
2	72 ± 6 nm

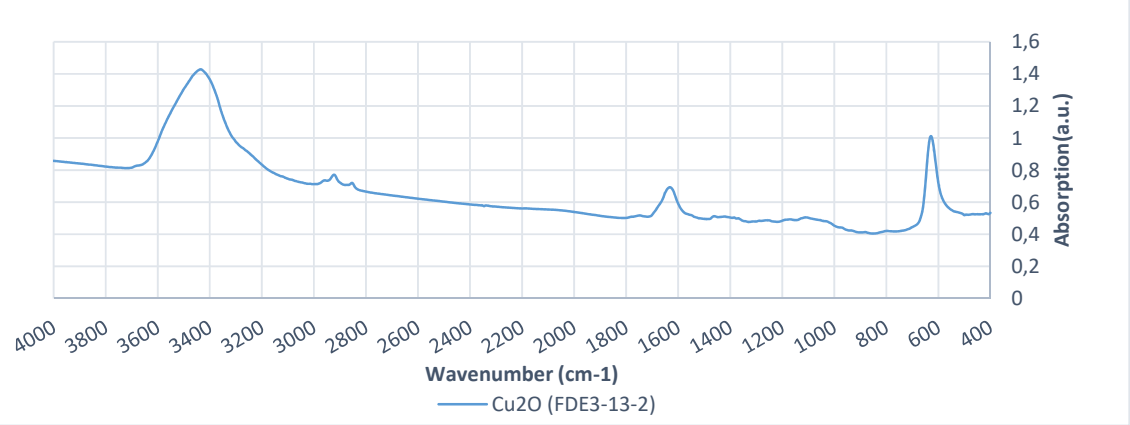

Figure 13: IR spectrum of cuprous oxide nanocubes.

4.1.2. Porous silica coating

Uniform coating

Ammonia is commonly used as base catalyst for the synthesis of MCM-41. However, since ethanolic ammonia dissolves the cuprous oxide template, a modified procedure had to be used. The coating of cuprous oxide cubes with porous silica was approached via three procedures which resulted in different nanoparticles. Representative TEM images of the obtained nanoparticles are displayed in Figure 14. For method A, using TMAH as the base catalyst and adding TEOS over time did result in silica coated particles, but the coating was not uniform. For method B, Using sodium hydroxide as the base catalyst and adding the TEOS over time resulted in damaged cubes without any silica coating. For method C, Using sodium hydroxide as the base catalyst and adding this over time resulted in cuprous oxide cubes with a more uniform silica coating.

If the sodium hydroxide was added over time (method C), no damaged cubes were observed, in contrast to with procedure B were the sodium hydroxide was added abruptly, while is similar amount of sodium hydroxide was used. This higher resilience against damage might originate from fresh silica having the time to provide a protective layer on the cuprous oxide cubes when the sodium hydroxide is added over time. Procedure C produced the coating with the most uniform thickness, no visible aggregation on TEM images, and the dispersions were colloidally stable. Based on these results, procedure C was chosen to produce the coatings for the particles studied here forth.

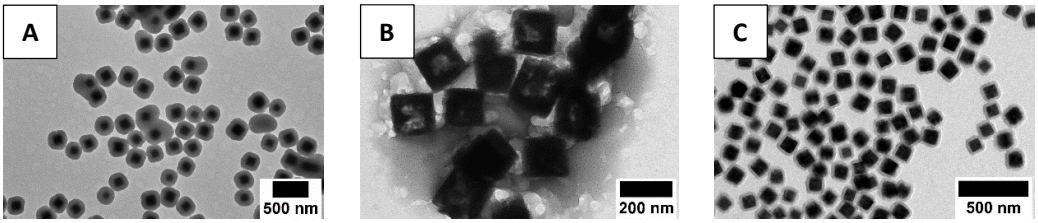

*Figure 14 Resulting nanoparticles from procedure A (**A**), B (**B**) and C (**C**)*

The absorption at 1070 and 455 cm^{-1} in the IR spectrum (displayed in Figure 15) confirm the silica coating on the cuprous oxide nanocubes.

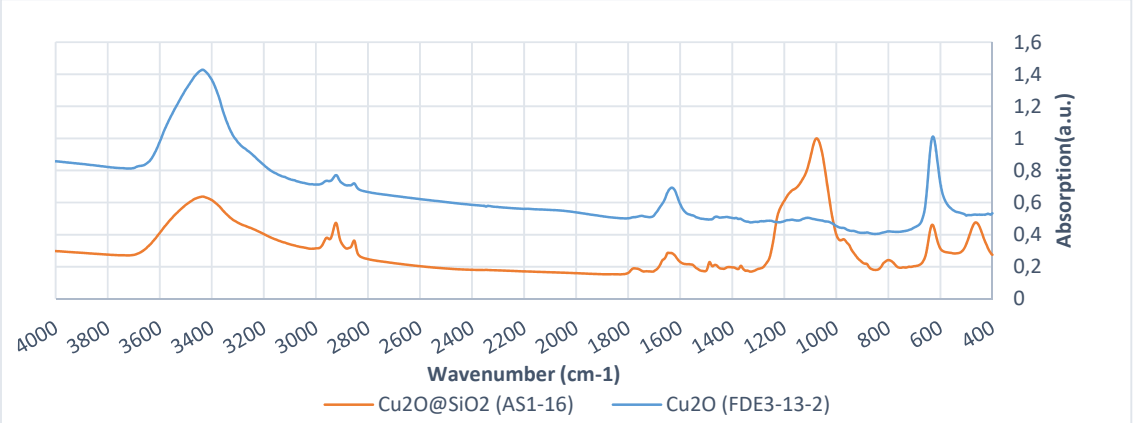

Figure 15: IR spectra of cuprous oxide nanoparticles before and after silica coating.

Controlling silica thickness

The thickness of the porous silica coating was controlled by varying the amount of TEOS present during the preparation. Mesoporous coatings with a thickness ranging from 13 to 63 nm were obtained by varying the added TEOS volume from 1 to 3 mL/mg cubes. TEM images of coated cuprous oxide cubes are shown in Figure 16.

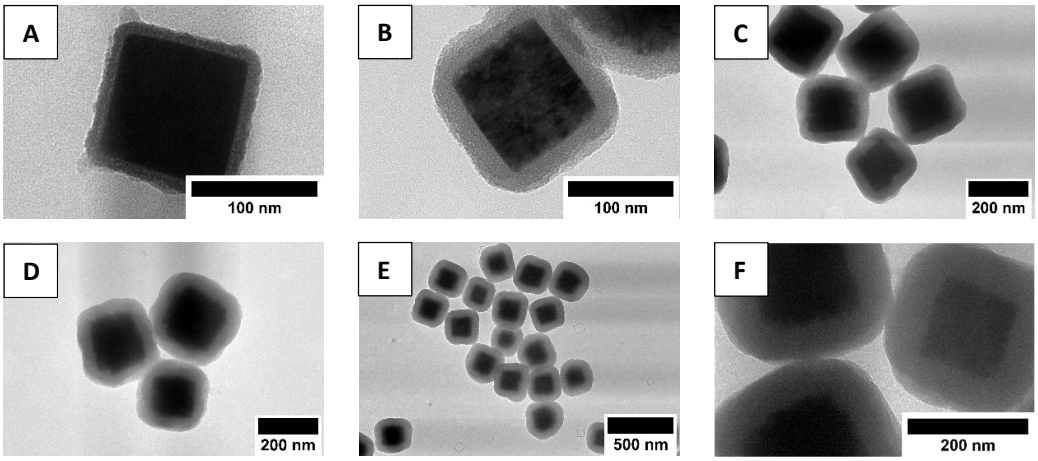

*Figure 16: TEM images of coated cubes produced with **A**: 1, **B**: 1.25, **C**: 1.5, **D**: 2, **E**: 2.5 and **F**: 3 mL/mg cubes. A clear increase in silica shell thickness is observed with increasing TEOS amounts.*

In Figure 17 the measured thickness of the obtained silica shells is depicted against the amount of TEOS added during coating. A clear trend is visible from Figure 17, showing an increase in coating thickness with increasing amount of added TEOS. Extrapolating the datapoints does not result in the line crossing at 0 nm at 0 mL/mg TEOS. The formation of a silica coatings seems to start around 0.8 mL/mg cubes. This suggests a certain (TEOS) concentration has to be reached before silica growth starts. Secondly, the silica layer doesn't double in thickness when the amount of TEOS is doubled. This is due to the layer thickness not being a perfect measure for the volume of silica deposited, since the volume of the three dimensional shell does not scale linearly with the shell thickness.

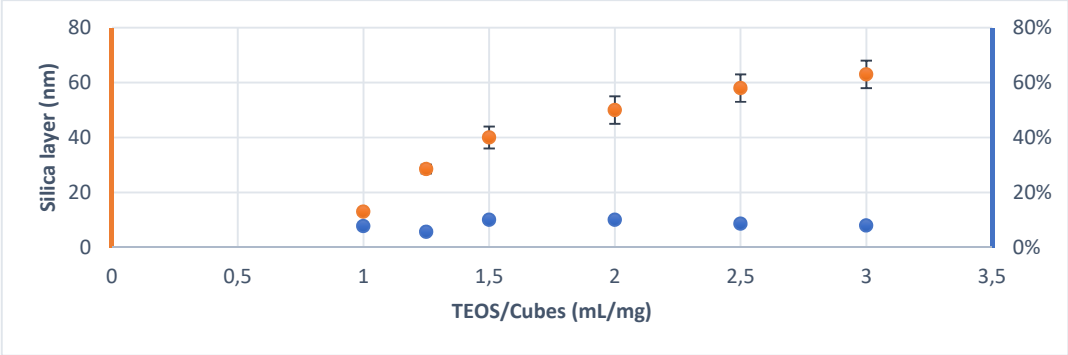

Figure 17: Plot of TEOS (mL/mg cubes) against the resulting coating thickness and relative standard deviation.

Upon examining the layer growth, trend two regimes can be identified. A thin layer regime (up to 1.5 mL/mg cubes), where the increase in silica volume is dominated by the linear volume increase of the six flat planes of silica. And an exponential regime (up from 1.5 mL/mg cubes), where the increase in silica volume is taken over by the volume on the eight silica corners. Together these eight corners roughly constitute a sphere, which volume grows with the measured shell thickness cubed. As shown in Figure 18, both regimes seem to adhere a linear trend. However, due to the amount of data points per regime, this can only be confirmed for the exponential regime.

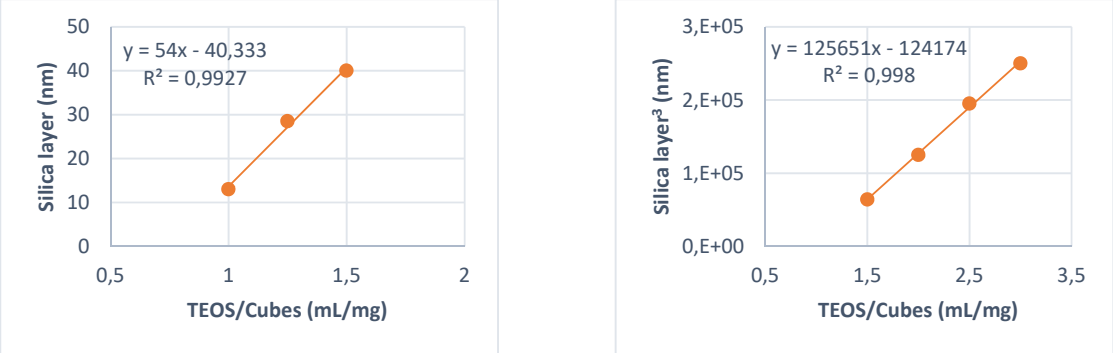

*Figure 18: Amount of TEOS (mL/mg cubes) plot against the silica layer (**left**) and the silica layer cubed (**right**).*

4.1.3. Porosity

To determine the porosity of the silica shell obtained with the CTAB template, the particles were first analyzed with TEM. In Figure 19 it is clearly visible that MCM-41 coating (left) contains mesopores in contrast to Stöber silica coating (right), which contains micropores which are not visible with the TEM. The TEM images show a distinct grain with a length scale of roughly 2-4 nm, which corresponds to the expected pore size[42].

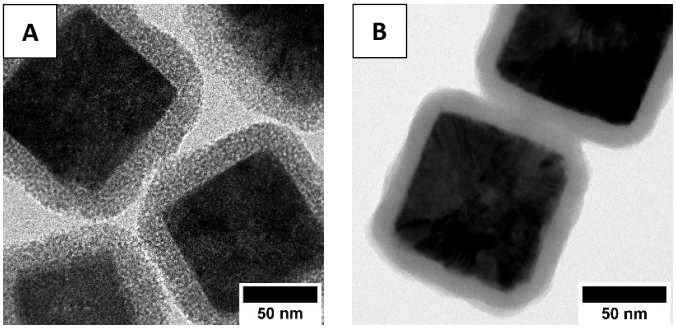

*Figure 19: TEM images of cuprous oxide cubes with **A**: Mesoporous silica coating, and **B**: Stöber silica coating.*

The density of the silica shell was estimated by calculating the volume of silica on an average nanocube and calculating the average volume of a cuprous oxide core. Comparing this to the weight increase upon coating and the known density of cuprous oxide the density could be estimated to be 0.8 g/cm^3. This is in excellent agreement with the 0.8 to 0.9 g/cm^3 found in literature[51]. Further insight into this estimation is given in Appendix A.

Nitrogen physisorption was used to determine the pore size and total surface area of the silica nanoboxes. In Figure 20, a nitrogen physisorption isotherm is visible of template extracted porous nanoboxes, showing clear hysteresis, as expected for particles containing mesopores. BJH Pore size distribution was found to have a peak around 2.3 nm. The BET surface area was determined to be 1,156 m²/g.

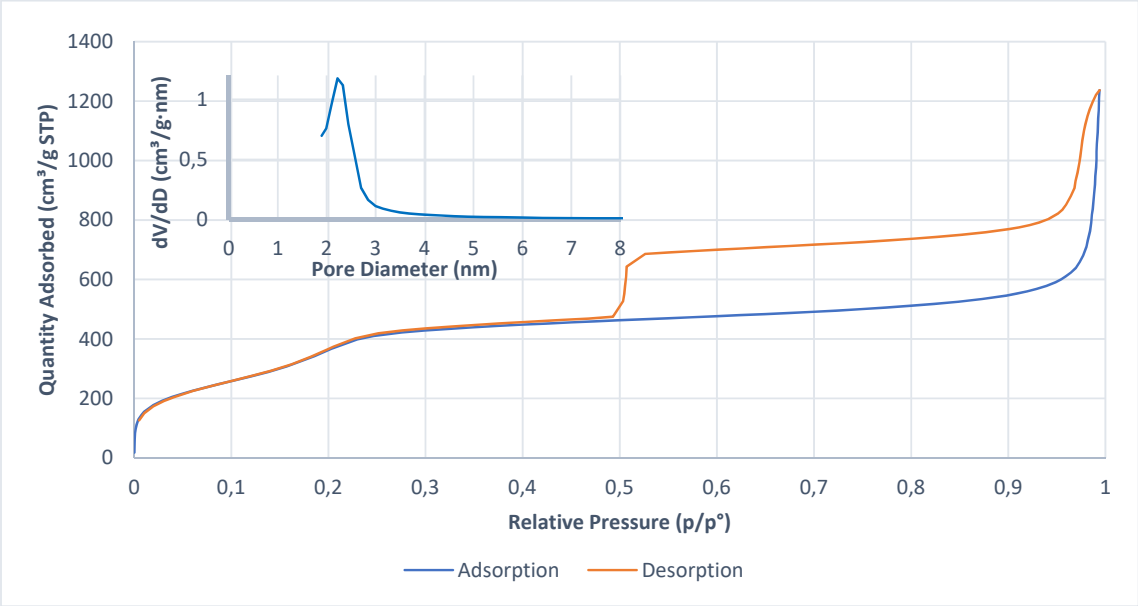

*Figure 20: **Main**: Nitrogen absorption isotherm of produced hollow nanoboxes. **Inset**: Pore size distribution.*

4.1.4. Template extraction

The CTAB and the cuprous oxide template were successfully extracted by refluxing in an ethanolic ammonium chloride solution as described in section 3.2.3. In Figure 21, it is visible that the core is fully removed and the shells seem to lose some structural rigidity after core removal. The resulting dispersions did retain a slightly brown color and did not become as white as pure silica.

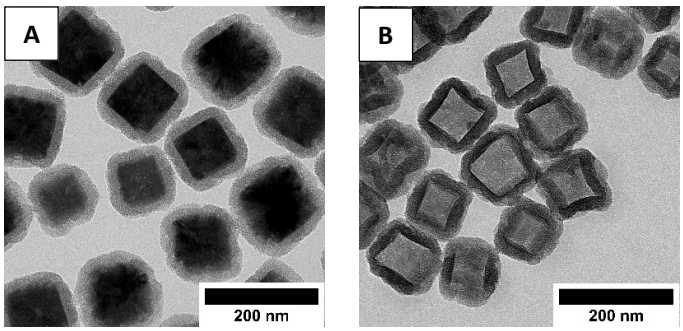

*Figure 21: TEM images before (**A**) and after (**B**) template extraction.*

The IR spectra in Figure 22 confirm the removal of the cuprous oxide core, visible from the absence of the cuprous oxide absorbance at 630 cm^{-1}. A small shoulder in the absorption is visible, suggesting not all cuprous oxide was removed. These low concentration cuprous oxide impurities are probably "stuck" in the silica matrix, as repeating the extraction did not yield samples of higher purity. This was earlier also observed for Cu_2O extraction from Stöber silica coated cuprous oxide core shell particles[13].

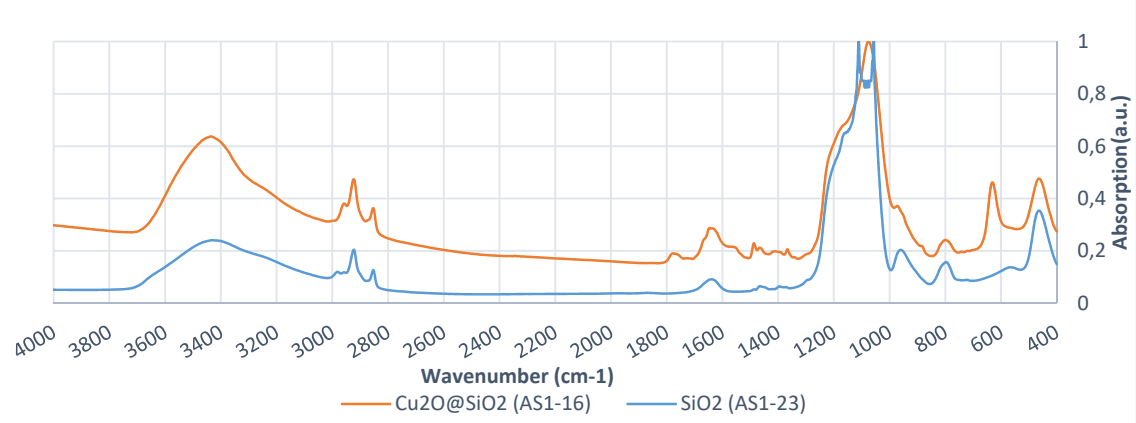

Figure 22: IR spectra before and after template extraction.

After the extraction of the cuprous oxide core from shells of 13 nm and thinner, TEM images show collapsed shells (Figure 23). It is suspected that the particles are dispersed as cubes, and collapse occurs during the drying of the colloids. During the drying of the core it is probable that the capillary interactions result in the collapse of the thinner, less rigid hollow nanoparticles.

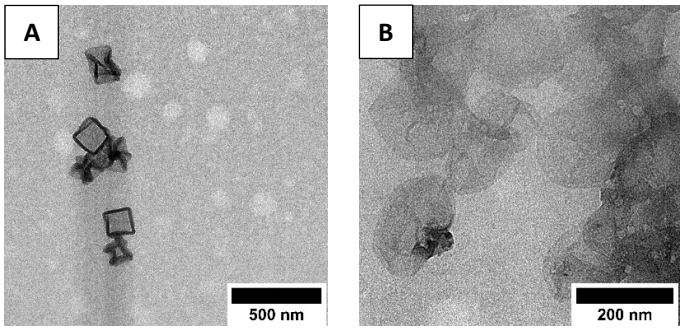

*Figure 23: TEM images showing the collapse of thin shell nanoparticles with a shell thickness of **A**: 13 nm and **B**: 1 - 2 nm.*

4.1.5. Hydrophobic surface modification

The surface of porous silica cubes was hydrophobized with TMS and HMDS as described in sections 3.2.4 and 3.2.5. Both procedures produced nanoparticles that are more stable in hexane than unmodified silica nanoboxes. The HMDS particles sediment slightly slower and are significantly easier to redisperse than the TMS particles. The modified particles are not as stable in hexane as unmodified particles are in ethanol. As a crude comparison, HDMS modified particles in hexane sediment in the course of hours, while unmodified particles in ethanol sediment in the course of days. The lower stability of HDMS modified particles in hexane when compared to unmodified particles in ethanol is likely due to lack of double layer repulsion. Modified particles are, however, more stable in hexane than unmodified particles in hexane, which sediment over the course of minutes. Figure 24 shows unmodified (left) and TMS modified (right) nanoparticles dispersed in equal parts hexane and water. After agitation and phase separation, the modified particles show a strong preference for the hexane phase. This in contrast to unmodified particles which prefer the interface and water phase.

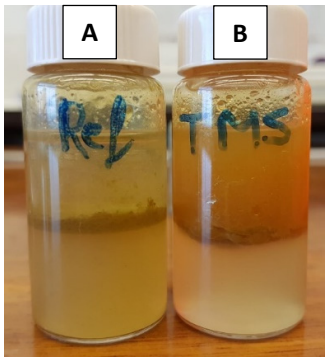

*Figure 24: Unmodified (**A**) and TMS modified (**B**) nanoparticles in hexane:water.*

4.2.Functional nanoboxes

4.2.1. Gold seed deposition

After treating hollow cubes with chloroauric acid/sodium borohydride solution according to section 3.3.1, the TEM images (Figure 25, A and B) of the produced nanoparticles showed small deposits (red circles) of high contrast material with a diameter of 5±1 nm. Larger deposits were also visible (yellow circle), as depicted in Figure 25 (left). Tilting the TEM grid revealed that the deposits are not located in the particle void but are deposited in and on the particle wall, the TEM tilt series images can be found in appendix B The dispersion itself turned purplish, caused by the surface plasmon resonance (SPR) of the gold particles.

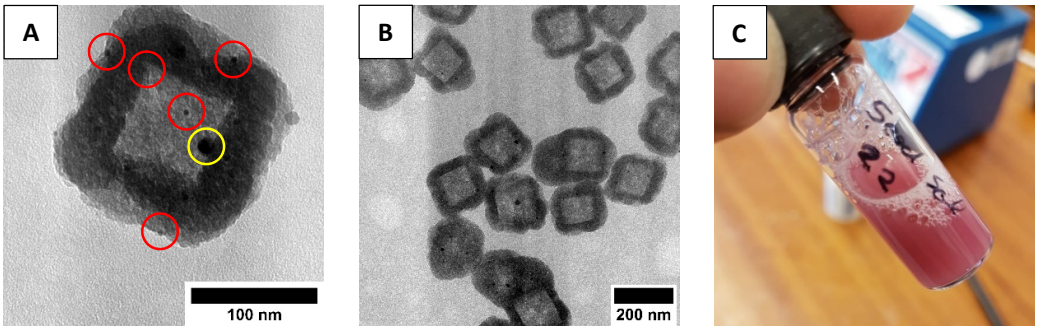

*Figure 25: **A**, **B**: TEM images of silica cubes with small gold deposits. **C:** Colored Dispersion.*

4.2.2. Quantum dot deposition

TEM image analysis of the produced dispersion showed that quantum dot synthesis was a success. The NaYF4:Yb,Er nanoparticles had an average size of 40 nm with a standard deviation of 1.4 nm. From TEM images (Figure 26) it is visible that the particles are spherical. However, no silica nanoboxes were observed, suggesting that the porous silica did not survive the quantum dot synthesis process. It is also possible that the cubes were in dispersion, but were not transferred during sample preparation.

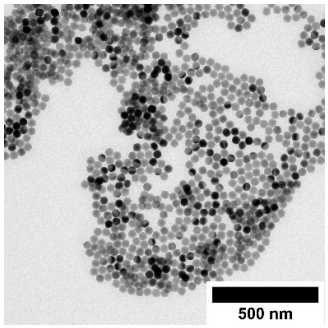

Figure 26: TEM image of the produced quantum dots.

4.2.3. Cuprous oxide disproportionation

Since seeded growth of functional particles inside the nanoboxes proved problematic, functional materials were deposited in the nanoboxes by transformation of the Cu_2O core. The cuprous oxide template coated with a 65 nm layer of silica could successfully be transformed by disproportionation with sulfuric acid. As visible in Figure 27, TEM images showed high contrast material, with dimensions significantly smaller compared to the original Cu_2O core, in most nanoboxes.

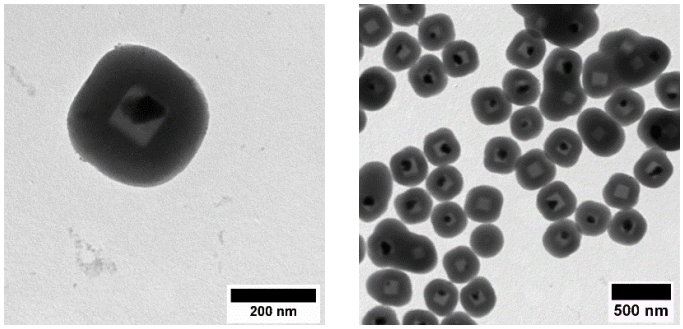

Figure 27: TEM images of $Cu@SiO_2$ nanoparticles produced by core disproportionation.

The disproportionation proceeds differently when attempted with cuprous oxide with a shell thinner than 40 nm. TEM images of the cubes appeared completely empty and while the color of the resulting sol was the same, it was noticed that the color evolution was different. In Figure 28 pictures taken before, during and after the reaction are presented. The mixture resulting in unsuccessful transformation, has a clear stage were neither cuprous oxide nor copper solids are present to color the mixture. The eventual color is slightly different, with the unsuccessful transformation having a slightly stronger red color. The evolution towards a red/purple color suggests copper nanoparticles are formed in both samples, however, the particles likely formed outside of the nanoboxes for unsuccessful disproportionation.

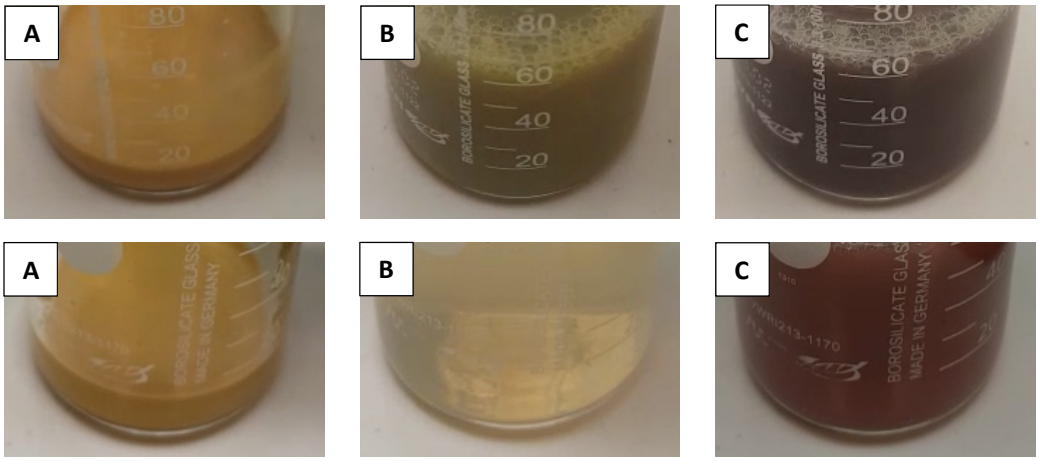

*Figure 28: Pictures taken before (**A**) during (**B**) and after (**C**) the disproportionation reaction of cuprous oxide in a thick (**top**) and thin (**bottom**) silica shell.*

It is suspected that a thick wall slows diffusion of the Cu^+ ion sufficiently to force the disproportionation and nanoparticle nucleation to occur inside the nanobox. Without the thick wall slowing down the Cu^+ diffusion, disproportionation and nucleation still seem to occur, but not necessarily inside the cubes.

4.2.4. Calcination

Calcination of silica coated cuprous oxide nanoparticles was attempted via two procedures. The first is calcination of dried particles under ambient atmosphere. The second is in-liquid calcination in TOPO under nitrogen atmosphere.

Air – Oven calcination

After oven calcination the nanoparticles were difficult to redisperse. Scraping and sonication were necessary to transfer a substantial amount of material into ethanol. The resulting dispersion was unstable and sedimented quickly, suggesting most particles were present as aggregates. TEM image analysis confirmed the presence of aggregates, as is shown in Figure 29 (left). Although single particles are visible, the majority of the sample is aggregated. Since prolonged periods of sonication did not increase stability and stop the rapid sedimentation of the sample, it is possible that the silica surfaces of adjacent cubes are fused together via condensation of open silanol groups. It is also possible that the sonication of the nanoboxes is too weak to disrupt the van der Waals attractive forces between the dried cubes. However, Since calcination increased the condensation of the silica removed organic material, the mesopores are more clearly visible on TEM images of calcined nanoboxes (Figure 29, middle an right).

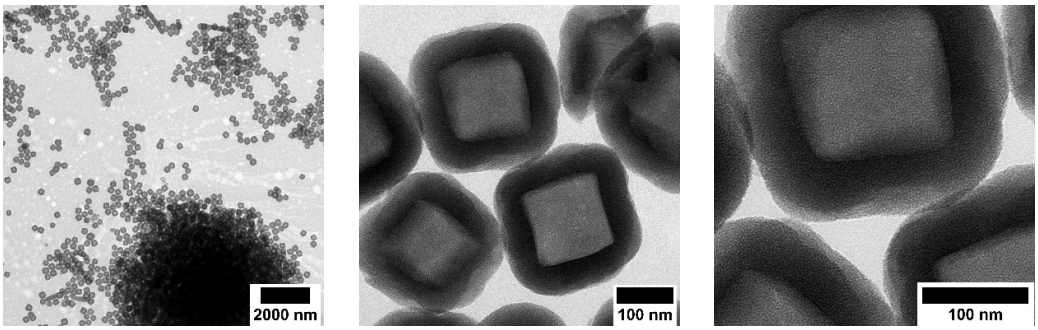

Figure 29: TEM images of hollow mesoporous cubes after oven calcination.

In liquid calcination

Stable dispersions were obtained via in liquid calcination, in contrast to oven calcination. Up to eight washing steps with water and ethanol were required to obtain these stable dispersions. It is suspected ionic impurities produced during calcination reduce the double layer repulsion in the unwashed dispersions. Washing removes these impurities, resulting in dispersions that are as stable as coated cuprous oxide dispersions. While in-liquid calcination was chosen to avoid the aggregation caused by oven calcination, this is not the only difference between the produced nanoparticles. TEM images (Figure 30, B) show that the nanoparticles no longer contain the cubic cuprous oxide template, compared to before in liquid calcination (Figure 30, A) or after dry calcination (Figure 30, C). The template was, due to prolonged heating under N_2 atmosphere, transformed into a smaller metallic copper core.

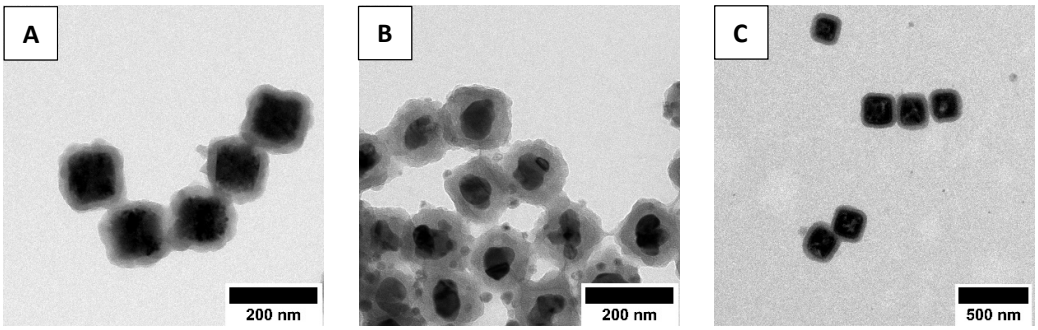

*Figure 30: TEM images of **A**: Uncalcinated particles, **B**: in liquid calcinated particles and **C**: oven calcinated particles.*

Samples taken during the calcination process showed a transformation from cuprous oxide to metallic copper. By comparing these samples visually (Figure 31), via TEM imaging (Figure 32) and via IR (Figure 33) the transformation could be followed. A primary component of the transformation seems to be the expulsion of oxygen from the cuprous oxide matrix. At elevated temperatures under nitrogen atmosphere, cuprous oxide nanoparticles are known to reduce to metallic copper nanoparticles via thermolysis[35]. The color evolution of the samples, from a cuprous oxide brown dispersion to a deep purple often seen for cupper nanoparticle dispersions, agrees with this hypothesis.

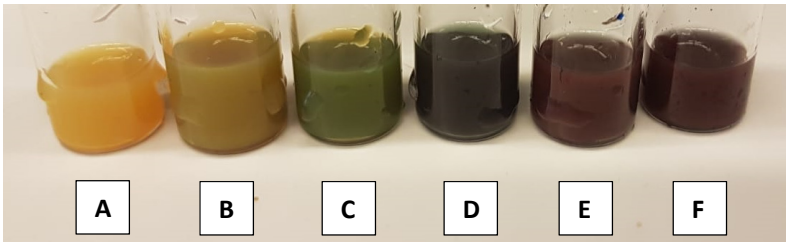

*Figure 31 Samples taken during the in liquid calcination process at 150 (**A**), 250 (**B**), 300 (**C**), 345 (**D**), 1hour at 350 °C (**E**) , and after cooling down (**F**).*

TEM imaging and IR analysis confirm the transformation from cuprous oxide to copper. At increasing temperature, the contrast of the core in TEM images (Figure 32), and the Cu-O peak in the IR spectrum (Figure 33 left) decreases in intensity, suggesting oxygen is removed from the core. The difference in contrast of the Cu_2O core at 150 °C and 250 °C becomes clear with a line scan, depicted in Figure 35, left.

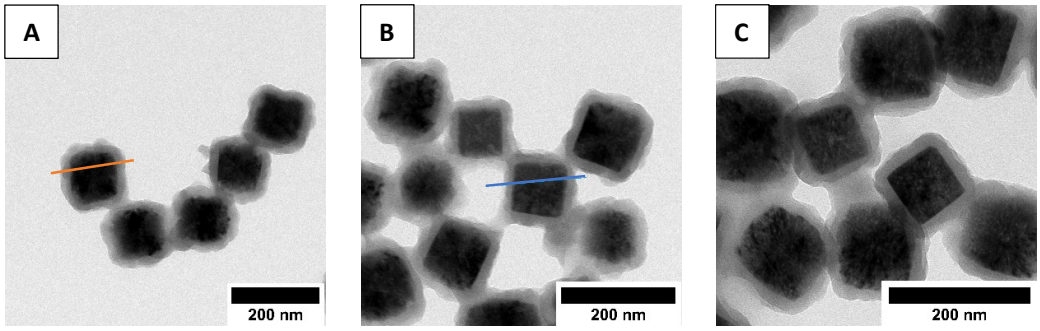

*Figure 32: TEM images of samples taken at 150 (**A**), 250 (**B**) and 300 °C (**C**).*

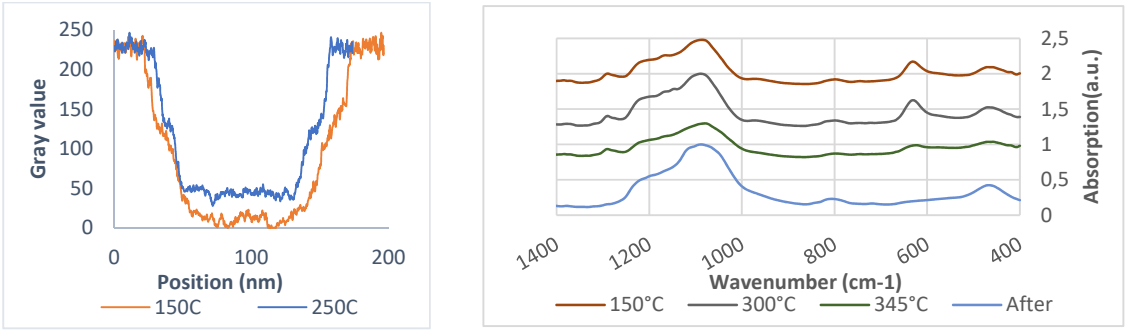

*Figure 33 **left**: gray value line scans of the lines in Figure 33 A and B. **Right**: normalized IR spectra of calcination samples, offset by 0.5 a.u. for clarity.*

Above 300 °C, the reduction process appears to be finished and a second process becomes apparent (Figure 34). Once the core mainly consists of metallic copper, the core starts to rearrange structurally. This can be explained by the melting effect of metallic copper nanoparticles. For copper particles of 40 nm, (surface) melting effects are known to emerge from as low as 200 °C[36]. After oxygen expulsion, the core consists of copper atoms distributed in the silica void. It is expected these copper atoms rearrange to minimize surface area.

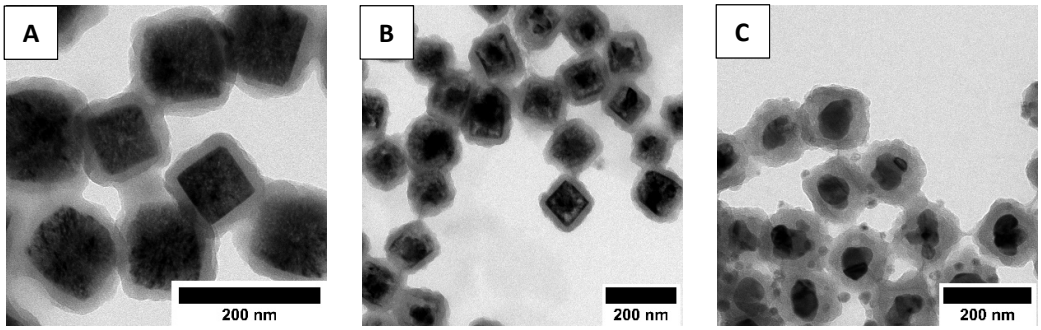

*Figure 34: TEM images of samples taken at 300 (**A**), 345 (**B**) and after one hour at 350 °C (**C**).*

Evaluation of the IR spectra also indicates an increase in the silica condensation after calcination as the ratio of the O-H to the Si-O peak significantly decreases. This is confirmed by the absence of the Si-OH peak after calcination, which was a weak but visible shoulder before calcination. While this increase was expected, the extend was not expected to be sufficient to significantly affect the IR spectrum[16]. In-liquid thermolysis thus proved to provide a route to produce well defined and stable Cu@SiO_2 nanobox dispersions.

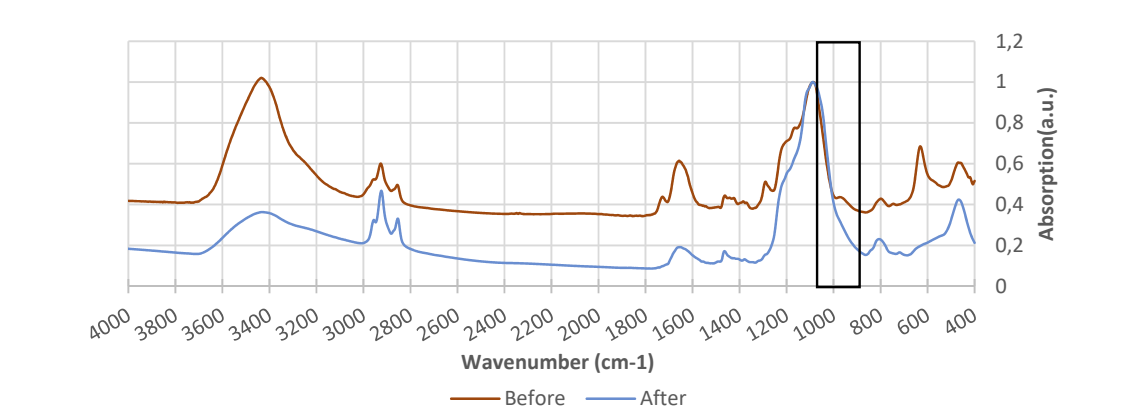

Figure 35: IR spectrum of particles before and after in liquid calcination.

4.2.5. Galvanic displacement

The metallic copper core of porous hollow nanocubes can be transformed into a silver or golden core via a galvanic displacement reaction. An important component of the procedure is the surface cleaning step with ascorbic acid. Without this preliminary step the galvanic displacement did not occur as intended. It is suspected that ascorbic acid reduces a layer of oxidized copper from the core, allowing the galvanic displacement to take place effectively. TEM images in Figure 36 show nanoparticles with a silver (A) and gold (B) core produced with galvanic displacement.

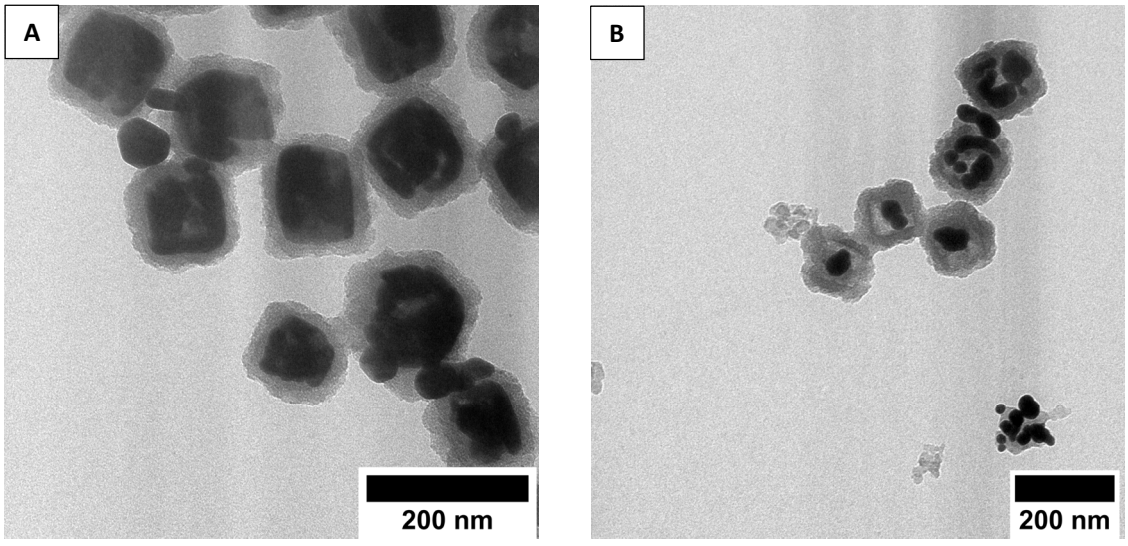

*Figure 36: **A**: Particles produced by displacement with silver. **B**: Particles produced by displacement with gold.*

The UV-Vis spectra of the particles with a silver and golden core, contain all the characteristic properties of the respective nanoparticles (Figure 37). The spectrum of the silver core is relatively flat in the visible region, since silver nanoparticles of circa 100 nm exhibit no sharp surface plasmon resonance[52]. The silver particle UV-Vis spectrum does however include a strong characteristic dip in absorption around 320 nm. The spectrum of particles with a gold core does show SPR-absorption around 570 nm. This absorption is a characteristic surface plasmon resonance peak that causes the reddish-purple appearance of colloidal gold dispersions.

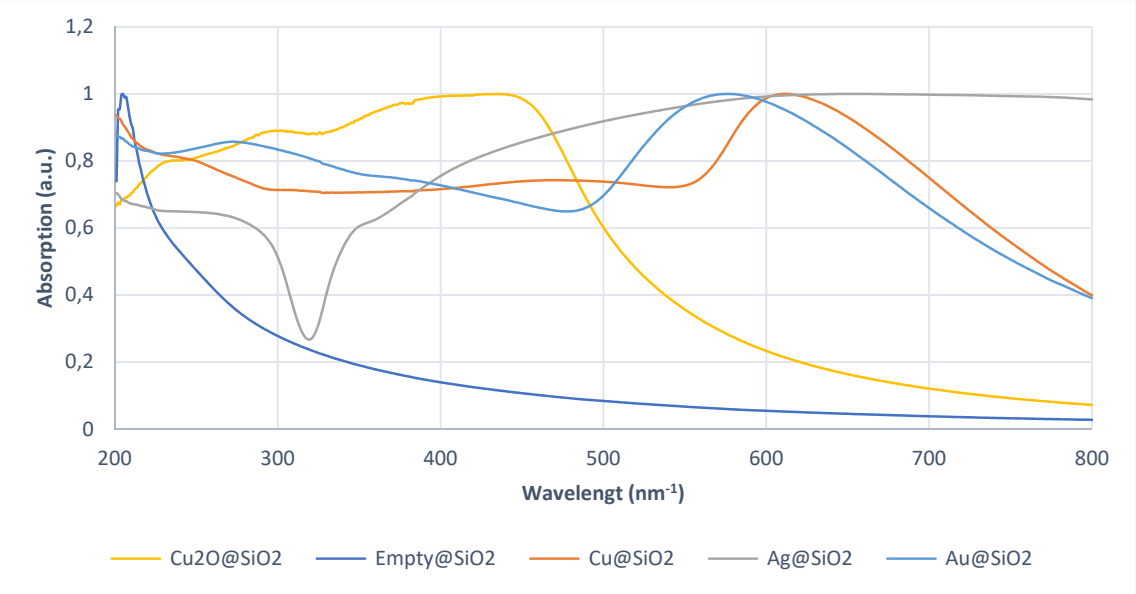

Figure 37: Normalized UV-Vis spectra of filled and empty nanobox dispersions.

The presence of the gold core could relatively easy be confirmed via a nitric acid test. Dispersions of silica nanoboxes with a copper or silver core rapidly lost their color upon addition to a nitric acid solution, while the dispersion with a gold core retained its purple/red color. The dissolution of Cu and Ag was also confirmed by TEM imaging, silica nanoboxes with previously had a copper or silver core were empty after treatment with nitric acid. The gold cores were still present after treatment with nitric acid. TEM images taken before and after nitric acid treatment can be found in appendix C.

4.2.6. EDX analysis

To confirm the composition of the core-shell nanoparticles, EDX-2D mapping was performed. In Figure 38, 2D-EDX maps obtained from a porous hollow nanocube with a silver core are presented. The EDX mapping confirms the core is indeed mainly composed of silver, while also showing trace amounts of copper present in the void. Since the copper map seems to overlap with the silver map, it is likely the copper is alloyed in with the silver core. The silicon and oxygen maps clearly show the silica cube enveloping the metallic core. The carbon map shows a trace amount of carbon, mainly concentrated on the metallic core. Sources of this carbon could be the CTAB used in coating or ascorbic acid from surface cleaning. From the HAADF and silver it is visible that the core fills the void in a peculiar way, covering most of the silica wall but leaving at least one wall uncovered. As discussed in section 2.3.4, these distinct shapes are commonly seen after galvanic displacement reactions and caused by the nanoscale Kirkendall effect[38,39].

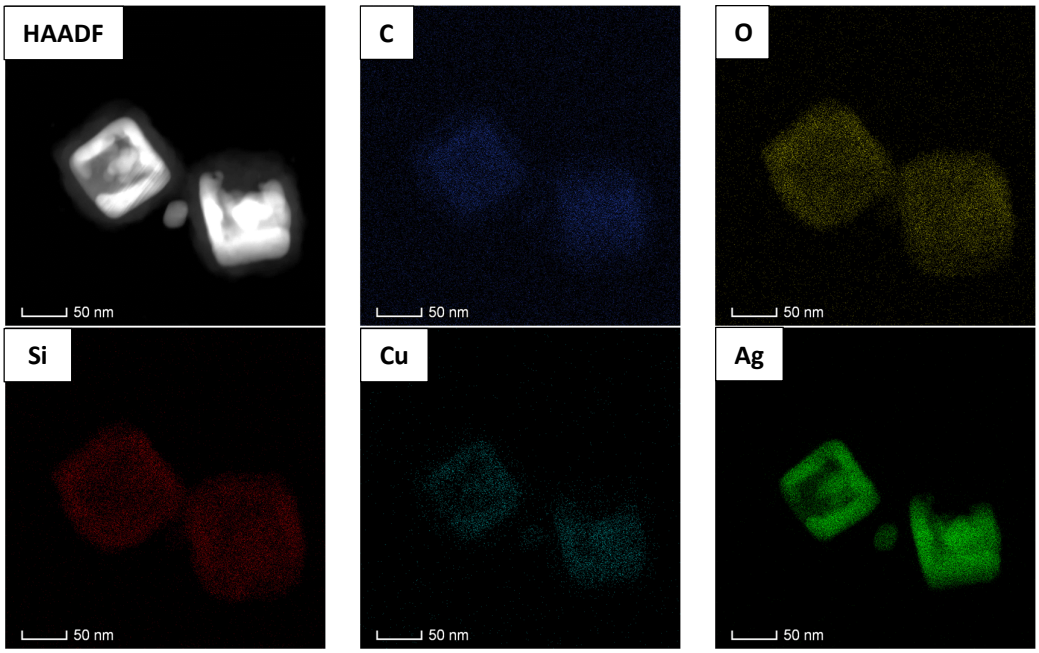

Figure 38: HAADF and EDX-2D elemental maps of Ag@SiO_2 nanoparticles.

From EDX-2D mapping of particles containing a gold core, the same general conclusions can be drawn with regard to the nanoboxes contain silver cores. In Figure 39, the set of images from a porous hollow nanocube with gold core are displayed. The core consists mainly of gold, with trace amounts of copper. The silica shell is clearly visible in the oxygen and silicon maps, and particle also contains carbon impurities. The gold core, when compared to the silver core, does not display any signs of the nanoscale Kirkendall effect. The absence of this effect is due to differences in the galvanic displacement process, notably the stoichiometry and metal in metal diffusion rates as discussed in section 2.3.4. In appendix D, larger, superimposed versions EDX maps are displayed.

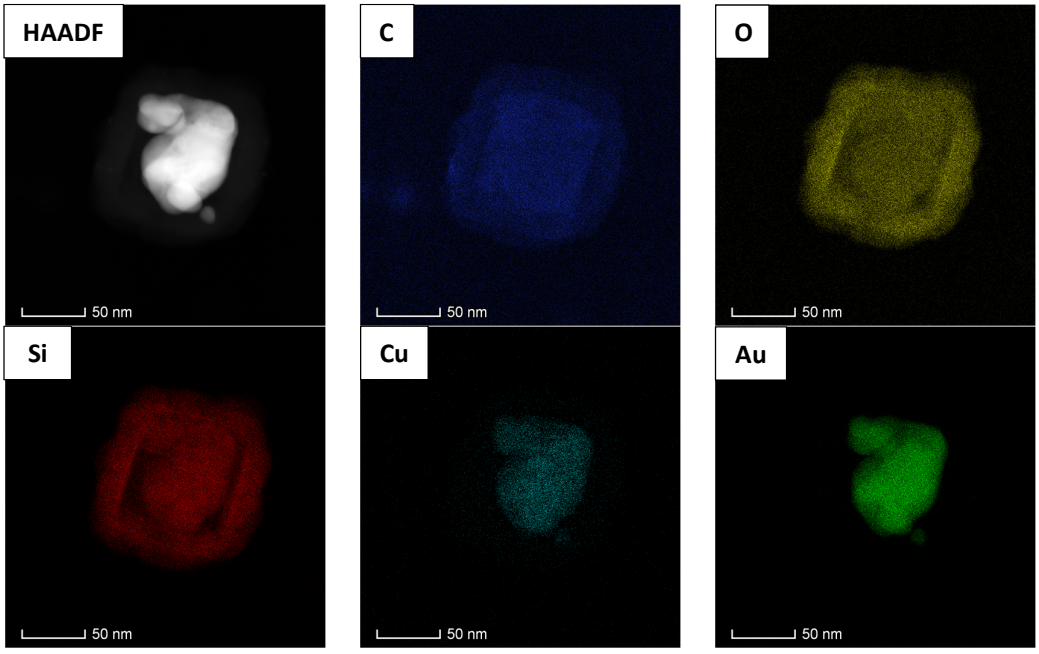

Figure 39: HAADF and EDX-2D elemental maps of Au@SiO_2 nanoparticles

4.2.7. Catalytic Congo red degradation by silver functionalized cubes

Now that the porous nanoboxes with a metal core are produced, their core functionality had to be confirmed. This was done by determining the catalytic activity as described in section 3.3.8. Catalytic activity for the degradation of congo red, of the silver core could easily be confirmed as the red color intensity of the mixture with added $Ag@SiO_2$ nanoparticles fully faded within 15 minutes, while the sample without cubes and the sample with empty cubes retained a strong red color. After two hours the sample with empty cubes also displayed a slight fading of color when compared to the reference sample (Figure 40, left). After removal of the nanoparticle degradation of the dye was confirmed with UV-Vis spectrometry (Figure 40, right and Table 6). Calculated from this limited dataset, the absorption intensity decreases slowly (0.05 A/hour) in the presence of sodium borohydride, and slightly faster (0.35 A/hour) in the presence of sodium borohydride and empty cubes. The degradation in the presence of sodium borohydride and $Ag@SiO_2$ nanoparticles, however, is significantly faster (5.2 A/hour). This not only confirms the catalytic activity of silver, but also shows that the shell is porous enough to allow for effective transfer of molecules.

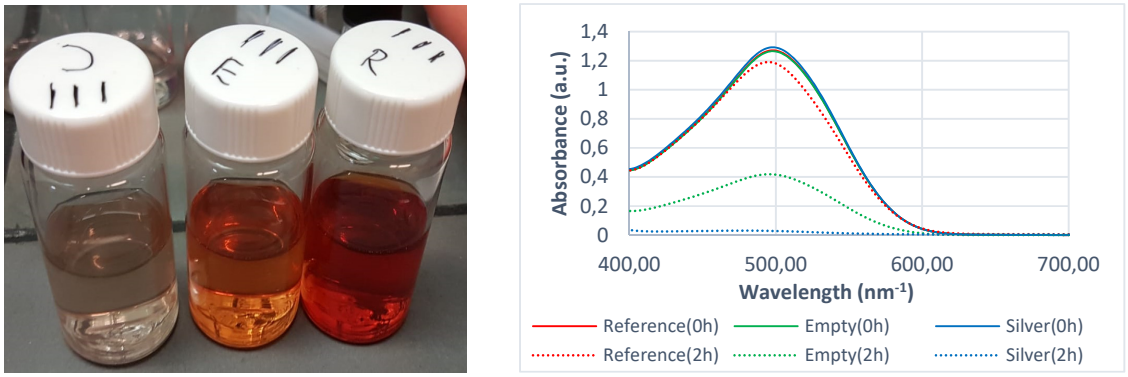

*Figure 40: **Left**: Sample vials after 2 hours. **Right**: Initial and final Visible light spectra.*

Table 6: Initial and final peak absorption per sample.

Sample	A_0	A_{2h}	A_{2h}/A_0	Rate (A/h)
Reference	1.2717	1.1905	93.61%	0.0812
Empty cubes	1.2653	0.4188	33.10%	0.8465
$Ag@SiO_2$	1.2922	0.0360	2.79%	5.0248

The precise rate of the reaction was successfully determined by following the progression on UV-Vis over time (Figure 41).

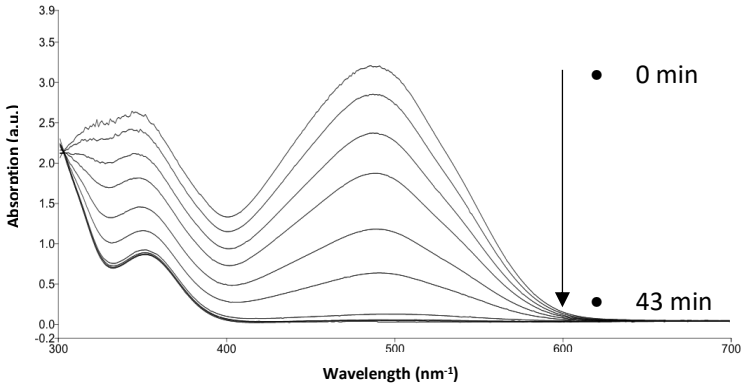

Figure 41 UV-Vis absorbance spectra of the dispersion at several timepoints. Not all spectra are plotted to preserve clarity. With the isosbestic point at 302 cm^{-1}.

When the absorbance of the peak (490 nm) is plotted against reaction time, the progress of the reaction can be divided into three main sections. (Figure 42, left). The first section, in red, is where the dye concentration is above the linear response region of the UV-Vis spectrophotometer and the data points were thus not taken into further consideration. In the other regimes, the absorption is linearly dependent on the dye concentration. The middle section, in blue, is where the absorption decrease linearly with time. In the blue section, the dye degradation rate is constant and independent of the dye or borohydride concentration, suggesting the rate is mainly dependent on a constant; the available catalytic silver surface. The final section, in green, is where the dye concentration has become low and the degradations depends on the dye concentration. The green section shows a logarithmic decrease and shows a linear trend on a logarithmic plot (Figure 42, right), corresponding to a concentration dependent reaction rate. As expected, the degradation rate is mainly depends on the concentration of the reaction component with the lowest relative concentration; the constant catalytic surface in the blue section, and the low dye concentration in the green section.

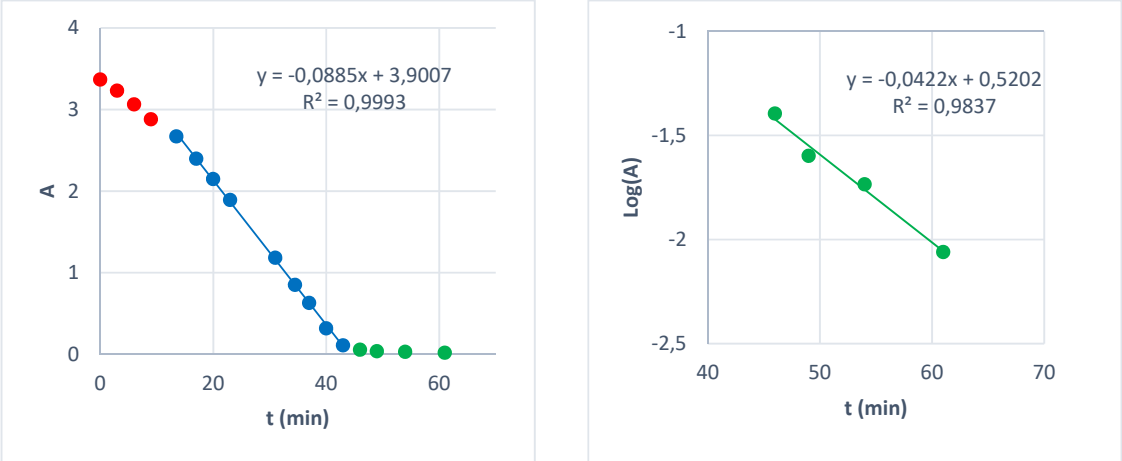

*Figure 42: Development of the peak absorption over time plot linear (**left**) and logarithmically (**right**).*

Plotting the degradation rate against the congo red concentration results in the plot in Figure 43, confirming the catalyst and congo red dependent rate regions. The plot clearly shows the zero order congo red rate dependence above circa 1 µmol/L and a first order dependence below circa 1 µmol/L. This suggests the reaction follows the Eley−Rideal mechanism as discussed in paragraph 2.4.3, but experiments with an order of magnitude higher dye concentration are required to confirm the reaction rate doesn't significantly decline with high dye concentration, and follows the Langmuir−Hinshelwood mechanism.

For the silica nanobox containing silver catalyst a degradation rate is obtained of 3.56E-07 mol/s·mg. This degradation rate per surface area is comparable to the catalytic degradation rates of Congo red found in literature for with 12 nm gold nanoparticles (6.57E-07 mol/s·mg)[53], and 20 nm silver nanoparticles (5.05E-07 mol/s·mg)[54].These result show the core is functional, and that the mesoporous shell does not significantly hinder the diffusion of the large organic dye molecule towards the functional core.

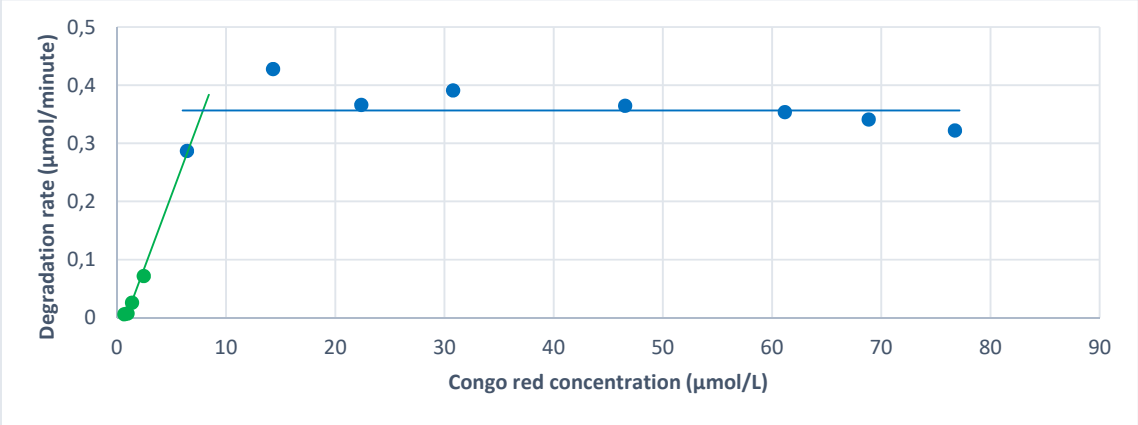

Figure 43: Degradation rate saturation effect.

5. Conclusion and outlook

Cubic cuprous oxide particles were successfully coated with mesoporous silica, using sodium hydroxide as a basic catalyst. Transmission electron microscopy and nitrogen physisorption confirmed that the silica layer had a high surface of circa 1150 m^2/g and contained mesopores of circa 2 nm. The thickness of the silica layer can be controlled by adjusting the concentration of tetra-ethyl-orthosilicate during the synthesis. In-liquid calcination proved to be successful, producing stable dispersions, in contrast to dry calcination. The stability of mesoporous nanoboxes in a polar solvents was improved by treatment with hexamethyldisilazane.

Gold seeds were deposited into mesoporous nanoboxes. The seeded growth approach did not result in monodisperse deposits, but the sample did display strong surface plasmon resonance absorption commonly observed for gold nanoparticles. It was attempted to deposit quantum dots into mesoporous nanoboxes, but no incorporated quantum dots were visible on TEM analysis. Using disproportionation and in-liquid thermolysis the cuprous oxide shape template was successfully transformed to metallic copper. In-liquid thermolysis provided a consistent route to transform the cuprous oxide encapsulated in silica shells. Using galvanic displacement, the copper core was substituted into a silver or gold core as confirmed by energy-dispersive X-ray spectroscopic mapping. The catalytic activity of $Ag@SiO_2$ functional nanoboxes towards the degradation of congo was determined using UV-VIS, showing similar catalytic activities compared to literature values.

The results presented here form the basis for the incorporation of functional materials inside nanoboxes. Further investigation could uncover paths to incorporate more complex materials in anisotropic core-shell particles. For example, it would be interesting to attempt the conversion of the template into photon up-conversion materials via cation exchange in combination with galvanic displacement. The incorporation of polymers via copper mediated living radical polymerization could also provide the possibility to deposit functional organic material in the silica nanobox.

6. Acknowledgements

To start, I would like to thank Frans for his supervision. Without your knowledge and ideas this project would not have been possible. You thought me the basics of colloidal synthesis, and were happy to spend full afternoons at the TEM looking at failed cubes. I think it is due to your supervision that I never truly felt lost during this project. Next, I would like to thank Albert for his ideas, supervision and teaching. The framework you built allowed for this project to progress. I would also like to thank Dominique, for providing an efficient lab environment, and for her sharp eye on the TEM. In general, I express my gratitude to the FCC lab, all staff and students included, for providing and supporting an excellent environment for research and education. For their assistance outside of FCC, I would like to thank Thomas van sweeten (CMI), and Remco Dalebout (ICC), for their assistance with respectively the quantum dot synthesis and the nitrogen physisorption measurements.

7. Bibliography

1. Gong J, Li G, Tang Z. Self-assembly of noble metal nanocrystals: Fabrication, optical property, and application. *Nano Today*. 2012;7(6):564-585. doi: 10.1016/j.nantod.2012.10.008.

2. Pablo F. Damasceno, Michael Engel, Sharon C. Glotzer. Predictive self-assembly of polyhedra into complex structures. *Science*. 2012;337(6093):453-457. doi: 10.1126/science.1220869.

3. Meijer JM, Pal A, Ouhajji S, Lekkerkerker HNW, Philipse AP, Petukhov AA. Observation of solid-solid transitions in 3D crystals of colloidal superballs. *Nature Communications Nature Communications*. 2017;8(1):14352. doi: 10.1038/ncomms14352.

4. Laura Rossi, Vishal Soni, Douglas J. Ashton, et al. Shape-sensitive crystallization in colloidal superball fluids. *Proceedings of the National Academy of Sciences of the United States of America*. 2015;112(17):5286-5290. doi: 10.1073/pnas.1415467112.

5. Tao AR, Habas S, Yang P. Shape control of colloidal metal nanocrystals. *Small*. 2008;4(3):310-325. doi: 10.1002/smll.200701295.

6. Kamata K, Lu Y, Xia Y. Synthesis and characterization of monodispersed core-shell spherical colloids with movable cores. *Journal of the American Chemical Society*. 2003;125(9):2384-2385. doi: 10.1021/ja0292849.

7. Stöber W, Fink A, Bohn E. Controlled growth of monodisperse silica spheres in the micron size range. *Journal of Colloid And Interface Science*. 1968;26(1):62-69. doi: 10.1016/0021-9797(68)90272-5.

8. Johnson PM, van Kats CM, van Blaaderen A. Synthesis of colloidal silica dumbbells. *Langmuir : the ACS journal of surfaces and colloids*. 2005;21(24):11510-11517. doi: 10.1021/la0518750.

9. Graf C, Vossen DLJ, Imhof A, van Blaaderen A. A general method to coat colloidal particles with silica. *Langmuir*. 2003;19(17):6693-6700. doi: 10.1021/la0347859.

10. Liu S, Lu L, Yang Z, Cool P, Vansant EF. Further investigations on the modified stöber method for spherical MCM-41. *Materials Chemistry and Physics*. 2006;97(2):203-206. doi: 10.1016/j.matchemphys.2005.09.003.

11. Kato N, Ishii T, Koumoto S. Synthesis of monodisperse mesoporous silica hollow microcapsules and their release of loaded materials. *Langmuir : the ACS journal of surfaces and colloids*. 2010;26(17):14334-14344. doi: 10.1021/la1024636.

12. Wang X, Feng J, Bai Y, Zhang Q, Yin Y. Synthesis, properties, and applications of hollow micro-/nanostructures. *Chem Rev*. 2016;116(18):10983-11060. doi: 10.1021/acs.chemrev.5b00731.

13. Dekker F, Tuinier R, Philipse A. Synthesis of hollow silica nanocubes with tuneable size and shape, suitable for light scattering studies. *Colloids and Interfaces*. 2018;2(4):44. doi: 10.3390/colloids2040044.

14. Xiao M, Zhao C, Chen H, Yang B, Wang J. “Ship-in-a-bottle” growth of noble metal nanostructures. *Advanced Functional Materials*. 2012;22(21):4526-4532. doi: 10.1002/adfm.201200941.

15. Luo Z, Zhang J, Luo T, Zhou J, Zhao X, Cai K. Hollow mesoporous silica nanoparticles facilitated drug delivery via cascade pH stimuli in tumor microenvironment for tumor therapy. *Biomaterials*. 2016;83:51-65. doi: 10.1016/j.biomaterials.2016.01.008.

16. Cauda V, Argyo C, Piercey DG, Bein T. “Liquid-phase calcination” of colloidal mesoporous silica nanoparticles in high-boiling solvents. *Journal of the American Chemical Society*. 2011;133(17):6484-6486. doi: 10.1021/ja1067492.

17. Raut HK, Ganesh VA, Nair AS, Ramakrishna S. Anti-reflective coatings: A critical, in-depth review. *Energy & Environmental Science*. 2011;4(10):3779. doi: 10.1039/c1ee01297e.

18. Dekker F. Anti-reflective coatings: Fundamentals and applications. .

19. Jose Antunes. Tamron 18-400mm: The all-in-one zoom. https://www.provideocoalition.com/tamron-18-400mm-one-zoom/. Updated 2017. Accessed June 21, 2019.

20. Wang Y, Su X, Ding P, Lu S, Yu H. Shape-controlled synthesis of hollow silica colloids. *Langmuir : the ACS journal of surfaces and colloids*. 2013;29(37):11575-11581. doi: 10.1021/la402769u.

21. Park JC, Kim J, Kwon H, Song H. Gram-scale synthesis of Cu2O nanocubes and subsequent oxidation to CuO hollow nanostructures for lithium-ion battery anode materials. *Advanced Materials*. 2009;21(7):803-807. doi: 10.1002/adma.200800596.

22. Guerrero-Martínez A, Pérez-Juste J, Liz-Marzán LM. Recent progress on silica coating of nanoparticles and related nanomaterials. *Advanced materials (Deerfield Beach, Fla.)*. 2010;22(11):1182-1195. doi: 10.1002/adma.200901263.

23. Van Blaaderen A, Van Geest J, Vrij A. Monodisperse colloidal silica spheres from tetraalkoxysilanes: Particle formation and growth mechanism. *Journal of Colloid And Interface Science*. 1992;154(2):481-501. doi: 10.1016/0021-9797(92)90163-G.

24. Kresge CT, Leonowicz ME, Roth WJ, Vartuli JC, Beck JS. Ordered mesoporous molecular sieves synthesized by a liquid chrystal template mechanism. *Nature*. 1992(359):710-712.

25. Prasomsri T, Jiao W, Weng SZ, Garcia Martinez J. Mesostructured zeolites: Bridging the gap between zeolites and MCM-41. *Chemical communications (Cambridge, England)*. 2015;51(43):8900-8911. doi: 10.1039/C4CC10391B.

26. Donohue MD, Aranovich GL. Adsorption hysteresis in porous solids. *Journal of Colloid And Interface Science*. 1998;205(1):121-130. doi: 10.1006/jcis.1998.5639.

27. Deekamwong K, Wittayakun J. Template removal by ion-exchange extraction from siliceous MCM-41 synthesized by microwave-assisted hydrothermal method. *Microporous and Mesoporous Materials*. 2017;239:54-59. doi: 10.1016/j.micromeso.2016.09.049.

28. Jabariyan S, Zanjanchi MA. A simple and fast sonication procedure to remove surfactant templates from mesoporous MCM-41. *Ultrasonics - Sonochemistry*. 2012;19(5):1087-1093. doi: 10.1016/j.ultsonch.2012.01.012.

29. Goncharuk O. The heat of immersion of modified silica in polar and nonpolar liquids. *J Therm Anal Calorim*. 2015;120(2):1365-1373. doi: 10.1007/s10973-015-4438-y.

30. Manca M, Cannavale A, De Marco L, Aricò AS, Cingolani R, Gigli G. Durable superhydrophobic and antireflective surfaces by trimethylsilanized silica nanoparticles-based Sol−Gel processing. *Langmuir : the ACS journal of surfaces and colloids*. 2009;25(11):6357-6362. doi: 10.1021/la804166t.

31. Alimunnisa J, Ravichandran K, Meena KS. Synthesis and characterization of Ag@SiO2 core-shell nanoparticles for antibacterial and environmental applications. *Journal of Molecular Liquids*. 2017;231:281-287. doi: 10.1016/j.molliq.2017.01.103.

32. Huy DX, Lee YB, Lee H, Choi WS. Rattle-type hierarchical particles containing multilevel cores (Ag@AgCl@SiO2 and au/Ag@AgCl@SiO2) as versatile catalysts. *Journal of Colloid And Interface Science*. 2014;425:178-185. doi: 10.1016/j.jcis.2014.02.037.

33. Castillo SIR. *Cubic colloids : Synthesis, functionalization and applications.* Utrecht University; 2015.

34. Jiang J, Kim S, Piao L. The facile synthesis of Cu@SiO2 yolk–shell nanoparticles via a disproportionation reaction of silica-encapsulated Cu2Onanoparticle aggregates. *The Royal Society of Chemistry*. 2015;7:8299-8303.

35. Gao L, Pang C, He D, Shen L, Gupta A, Bao N. Synthesis of hierarchical nanoporous microstructures via the kirkendall effect in chemical reduction process. *Scientific reports*. 2015;5(1):16061. doi: 10.1038/srep16061.

36. Yeshchenko OA, Dmitruk IM, Alexeenko AA, Dmytruk AM. Size-dependent melting of spherical copper nanoparticles embedded in a silica matrix. *Physical Review B*. 2007;75(8). doi: 10.1103/PhysRevB.75.085434.

37. Alia SM, Yan YS, Pivovar BS. Galvanic displacement as a route to highly active and durable extended surface electrocatalysts. *Catal. Sci. Technol*. 2014;4(10):3589-3600. doi: 10.1039/C4CY00736K.

38. El Mel A, Nakamura R, Bittencourt C. The kirkendall effect and nanoscience: Hollow nanospheres and nanotubes. *Beilstein journal of nanotechnology*. 2015;6(1):1348-1361. doi: 10.3762/bjnano.6.139.

39. See Wee Chee, Shu Fen Tan, Zhaslan Baraissov, Michel Bosman, Utkur Mirsaidov. Direct observation of the nanoscale kirkendall effect during galvanic replacement reactions. *Nature Communications*. 2017;8(1):1-8. doi: 10.1038/s41467-017-01175-2.

40. Brunauer S, Emmett PH, Teller E. Adsorption of gases in multimolecular layers. *Journal of the American Chemical Society*. 1938;60(2):309-319. doi: 10.1021/ja01269a023.

41. Barrett EP, Joyner LG, Halenda PP. The determination of pore volume and area distributions in porous substances. I. computations from nitrogen isotherms. *Journal of the American Chemical Society*. 1951;73(1):373-380. doi: 10.1021/ja01145a126.

42. Nastase S, Bajenaru L, Berger D, et al. Mesostructured silica matrix for irinotecan delivery systems. *cent eur j chem*. 2014;12(8):813-820. doi: 10.2478/s11532-014-0501-y.

43. Merck KGaA. Silica, mesostructured, MCM-41 type (hexagonal). https://www.sigmaaldrich.com/catalog/product/aldrich/643645?lang=en&region=NL. Accessed June 21, 2019.

44. Ruiz-Zepeda F, Gatalo M, Jovanovič P, et al. Gold doping in PtCu3/HSAC nanoparticles and their morphological, structural, and compositional changes during oxygen reduction reaction electrochemical cycling. *ChemCatChem*. 2017;9(20):3904-3911. doi: 10.1002/cctc.201700690.

45. Naseem K, Farooqi ZH, Begum R, Irfan A. Removal of congo red dye from aqueous medium by its catalytic reduction using sodium borohydride in the presence of various inorganic nano-catalysts: A review. *Journal of Cleaner Production*. 2018;187:296-307. doi: 10.1016/j.jclepro.2018.03.209.

46. Murugan E, Shanmugam P. Surface grafted hyper-branched polyglycerol stabilized ag and AuNPs heterogeneous catalysts for efficient reduction of congo red. *Journal of nanoscience and nanotechnology*. 2016;16(1):426-438. doi: 10.1166/jnn.2016.10655.

47. Baxter RJ, Hu P. Insight into why the Langmuir–Hinshelwood mechanism is generally preferred. *The Journal of Chemical Physics*. 2002;116(11):4379-4381. doi: 10.1063/1.1458938.

48. Wang Y, Wu G, Yang M, Wang J. Competition between Eley–Rideal and Langmuir–Hinshelwood pathways of CO oxidation on cun and CunO (n = 6, 7) clusters. *The Journal of Physical Chemistry C*. 2013;117(17):8767-8773. doi: 10.1021/jp3122775.

49. Robberts GW, Statterfield CN. Effectiveness factor for porous catalysts; langmuir-hinselwood kinetic expressions for bimolecular surface reactions. *Dep. of Chem. Eng.* 1966.

50. Stewart IE, Ye S, Chen Z, Flowers PF, Wiley BJ. Synthesis of Cu–Ag, Cu–Au, and Cu–Pt Core–Shell nanowires and their use in transparent conducting films. *Chemistry of Materials*. 2015;27(22):7788-7794. doi: 10.1021/acs.chemmater.5b03709.

51. Zhao D, Wan Y, Zhou W. *Ordered mesoporous materials.* Weinheim: Wiley-VCH; 2013:510-511.

52. Steven J. Oldenburg. Silver nanoparticles: Properties and applications. https://www.sigmaaldrich.com/technical-documents/articles/materials-science/nanomaterials/silver-nanoparticles.html. Accessed Mar 3, 2019.

53. Ganapuram BR, Alle M, Dadigala R, Dasari A, Maragoni V, Guttena V. Catalytic reduction of methylene blue and congo red dyes using green synthesized gold nanoparticles capped by salmalia malabarica gum. *Int Nano Lett*. 2015;5(4):215-222. doi: 10.1007/s40089-015-0158-3.

54. Rajesh R, Kumar SS, Venkatesan R. Efficient degradation of azo dyes using ag and au nanoparticles stabilized on graphene oxide functionalized with PAMAM dendrimers. *New Journal of Chemistry*. 2014;38(4):1551. doi: 10.1039/c3nj01050c.

Appendix A – Mesoporous silica density estimation

The density of the mesoporous silica covering the cuprous oxide core was calculated by making use of the volume and mass ratios. The mass ratio between the core and the shell was determined by determining the solid mass of a sample before and after cuprous oxide template extraction. Determination of the volume ratio was less trivial, as a 3D model (Figure 44) of the cube had to be estimated from TEM images. By simplifying the superball shape into a set of simple geometric elements, the volume ratio can easily be determined. The core is a cube with an edge length of 93 nm. The Silica shell consists out of three elements. Firstly, six slabs, with an edge length of 93 nm and a thickness of 23 nm, emerging from the core cube faces. Secondly, twelve quarter cylinders, 3 cylinders total, with a length of 93 nm and a radius of 23 nm, emerging from the core cube vertices. And lastly, a set of one eighth partial spheres, together comprising full sphere with a radius of 23 nm. Besides the simplified geometry, the calculation assumes no significant amount of cubes is lost during cuprous oxide template extraction.

Table 7: Element parameters.

Color	Element	Description (nm^3)	Volume (nm^3)	Amount
Red	Core	96x96x96	884736	1
Yellow	Slab	96x96x23	211968	6
Green	Cylinder	96x23x23xπ	159543	3
Purple	Sphere	23x23x23x4/3xπ	50965	1

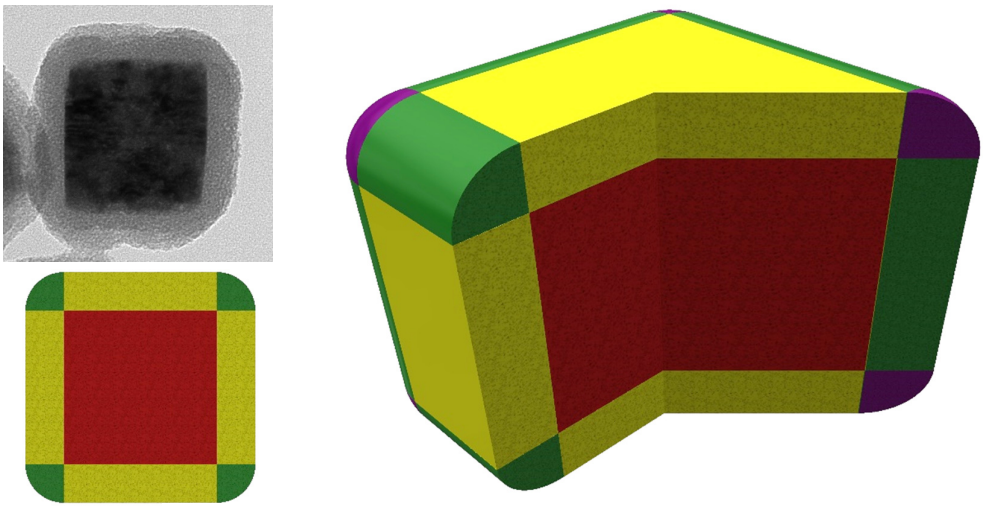

Figure 44: Sample TEM image, model half cut, and model open.

As visible in Table 8, there is roughly twice the volume of silica, while there is almost 4 times less mass. Combining these factors leads to a density ratio of 7.64. This ratio, combined with the known density of cuprous oxide allows the calculation of the mesoporous silica density. The resulting density, 0.79 g/cm^3, is in agreement with the 0.8 to 0.9 g/cm^3 found in literature[51].

Table 8 The resulting volume, weight and density ratios.

	Volume	Mass	Density
Core	884736 nm^3	150 mg	6.00 g/cm^3
Silica	1801401 nm^3	40 mg	**0.79** g/cm^3
Ratio	0.49	3.75	7.64

Appendix B – Gold deposition tilt series

No tilt TEM image – Gold deposit (yellow circle) appears inside the box due to the 2D transmission image

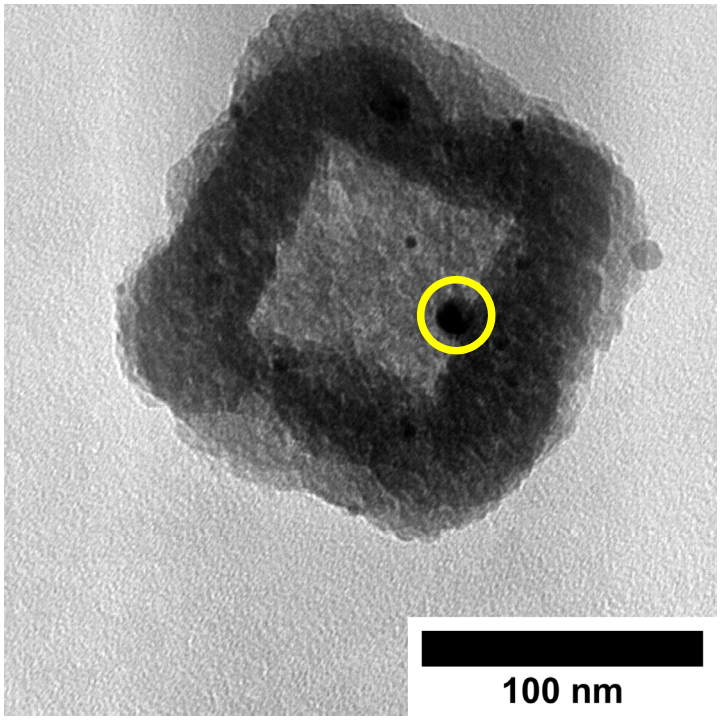

Tilted 30 degrees TEM image – Gold deposit is revealed to be either in or outside of the box wall

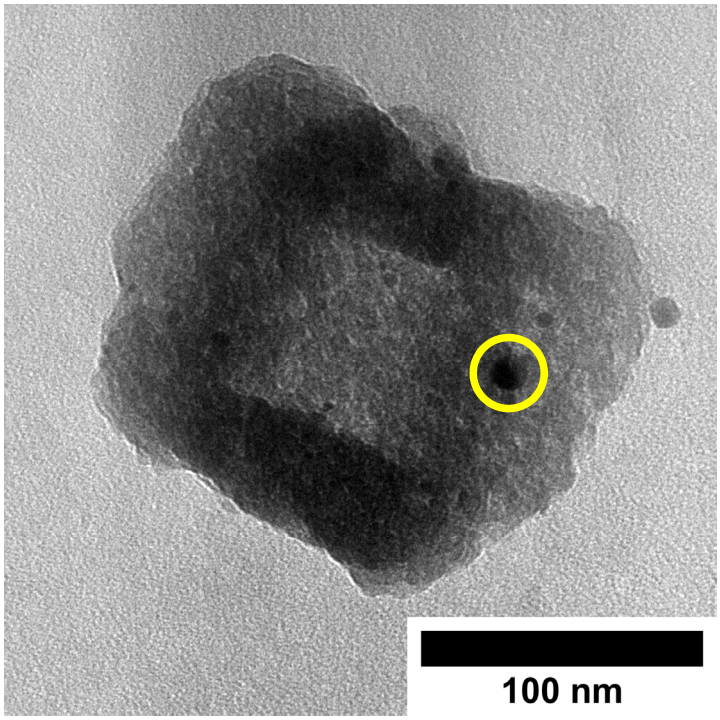

Appendix C – Acid test TEM images

TEM images of Metal@Si_2O cubes before (left) and after (right) acid treatment

Particles with a copper core are <u>empty</u> after nitric acid treatment

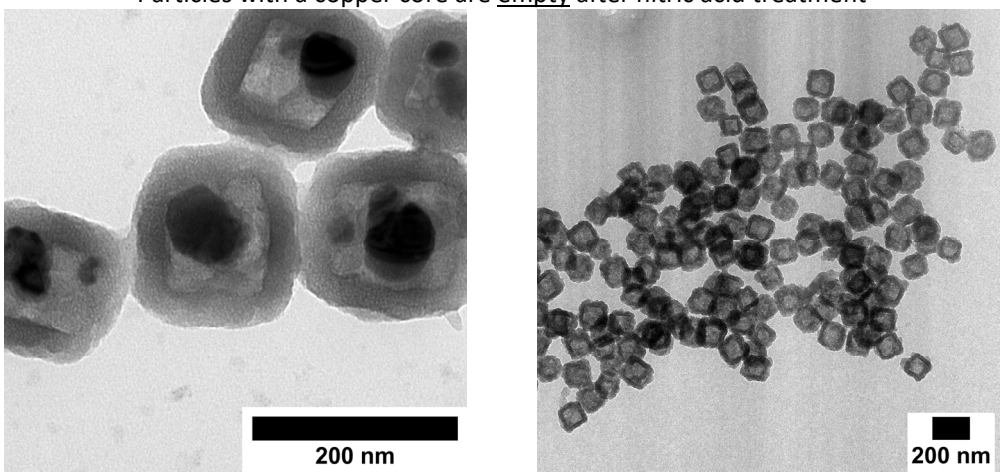

Particles with a silver core are <u>empty</u> after nitric acid treatment

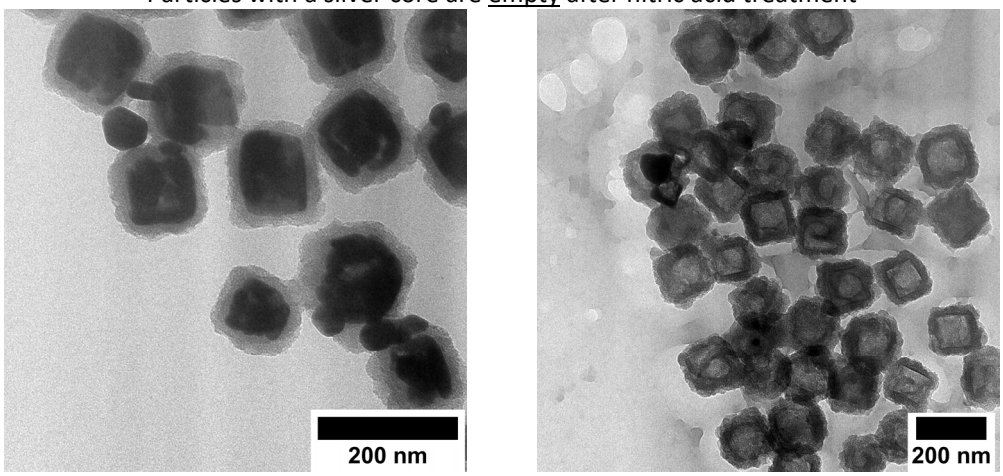

Particles with a silver gold are <u>not significantly changed</u> after nitric acid treatment

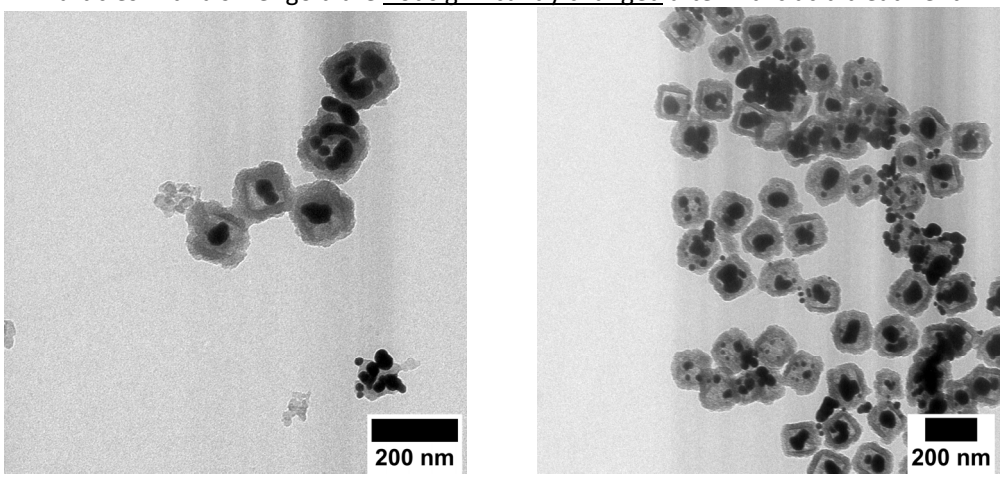

Appendix D – Superimposed EDX maps

Ag@SiO₂

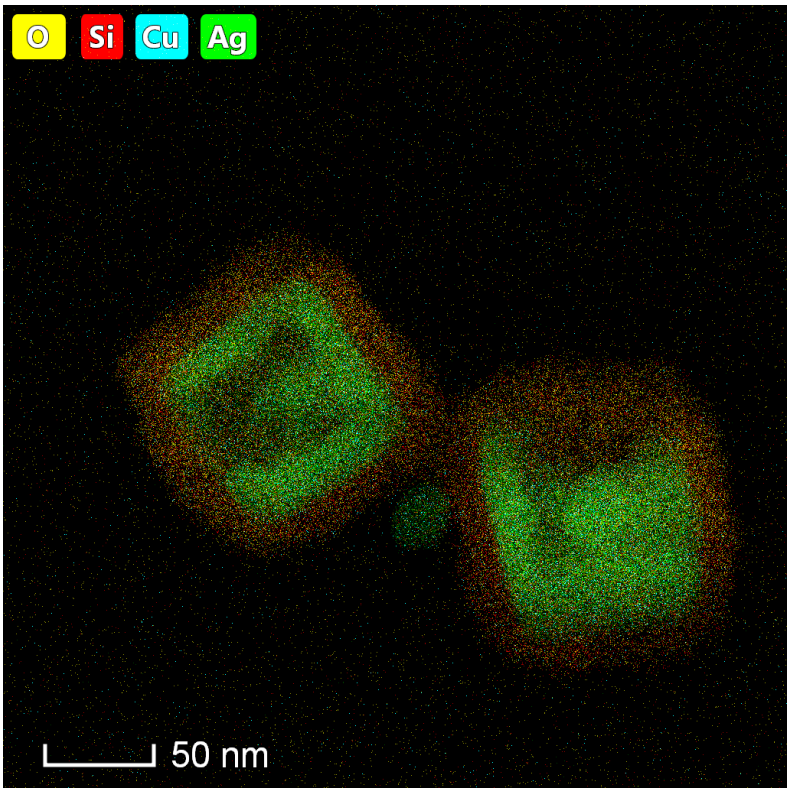

Au@SiO₂